Global distribution and environmental correlates of marine bioturbation

Shuang Zhang[1,2]*, Martin Solan[3], Lidya Tarhan[2]**

[1]Department of Oceanography, Texas A&M University, 3146 TAMU, College Station, TX 77843, USA.

[2]Department of Earth and Planetary Sciences, Yale University, P.O. Box 208109, New Haven, CT 06520, USA.

[3]Ocean and Earth Science, National Oceanography Centre Southampton, University of Southampton, Waterfront Campus, European Way, Southampton, SO14 3ZH, UK.

Correspondence: *shuang-zhang@tamu.edu; **lidya.tarhan@yale.edu

Paper's lead contact: shuang-zhang@tamu.edu

X (formerly Twitter): @caceelab (https://twitter.com/caceelab)

Summary

The activities of marine sediment-dwelling invertebrates play a fundamental role in mediating major biogeochemical cycles and have profoundly shaped the evolution of marine systems. Yet there remains a paucity of global marine data describing bioturbation intensities and mixed layer depths, and interrogating how these vary with multiple environmental and ecological factors at a system scale. We applied an ensemble of tree-based machine-learning techniques to resolve a global map and determine the environmental and ecological correlates most closely associated with bioturbation. We find that bioturbation intensity and the depth of the sediment mixed layer each reflect different associations with a consortium of environmental and ecological parameters, and that bioturbation intensities are much more readily predicted than sediment mixed layer depths from these correlates. Further, we find that the bioturbation intensity, the depth of the sediment mixed layer, and their environmental and ecological correlates differ between shallow marine and open-ocean settings. Our findings provide new insights into the importance of potential drivers of ancient sediment mixing recorded by geologic archives. These results also highlight that climate change may, in the near future, drive shifts in bioturbation and reciprocal fundamental changes in benthic functioning.

Introduction

Marine sediments form one of the largest and most diverse habitats on Earth and have been critical in regulating global carbon and nutrient cycling both in the modern oceans[1,2] and across geological timescales[3,4]. The presence and ecological complexity of communities of burrowing invertebrate fauna are closely associated, in seafloor settings today, with deep and intensive sediment particle mixing which, in turn, directly influences biogeochemical cycling (including of carbon and major macronutrients) as well as both seafloor and water-column ecology[5–8]. Similarly, the emergence and diversification of ancient bioturbators—burrowing and sediment-mixing animals—have been inferred to have shaped the evolution of biogeochemical cycling in Earth's past oceans[9–13]. Yet, despite mounting concern over the extent of biodiversity loss throughout the global ocean[14,15], there is currently limited understanding of how bioturbating animals—and the ecosystem and biogeochemical services they provide—will fare under future climate change in human-modified environments[16–18]. Understanding of how biodiversity and environmental crises will either impact or be amplified by future changes in bioturbation in the modern ocean has been hampered, foremost, by the absence of a robust quantitative framework to reconstruct the global scope of faunal bioturbation activities. Resolving this gap, however, is necessary to determine system responses to planetary change and, at local to regional scales, is critical to setting and implementing management and conservation benchmarks related to biodiversity, climate regulation, food security and other policy-relevant arenas[19].

Investigators have previously sought to identify the environmental and ecological parameters that exert control over faunal bioturbation intensity and sediment mixed layer depth by relating collated measurements of these processes to specific environmental parameters, such as water depth, freshwater discharge, dissolved oxygen levels, sedimentation rates, regional productivity

and availability of sedimentary organic matter[20–28]. However, these analyses have tended to employ relatively small subsets of available data[29,30], consider a limited number of environmental parameters[21,23], and rely on extrapolated correlations at coarser spatial scales that exclude regional variations in physical, chemical and ecological conditions[31,32]. Yet an extensive body of work has established that the contributions sediment-dwelling species make to ecosystem functioning are directly moderated by both biotic and abiotic local factors[33–36], including changes in anthropogenic behavior[37], which can fundamentally change the character of seafloor habitats and require the implementation of local rather than generic conservation and management strategies[38].

Here, we used machine learning to determine the primary environmental and ecological parameters that most strongly predict, and potentially control, variations in bioturbation processes across the modern seafloor. Additionally, we used these data to generate global maps of bioturbation intensity and sediment mixed layer depth at 5-minute spatial resolution. The bioturbation variables we consider include the biodiffusion intensity coefficient (Db, $cm^2\ yr^{-1}$)—an indicator of biological mixing intensity—and the depth of the sediment mixed layer (L, cm), collected across a spectrum of contemporary marine environments and representing the most extensive bioturbation dataset currently available[30] (see "Methods"). We combined these data with a similarly georeferenced environmental and ecological dataset, encompassing a wide variety of parameters from surface waters, bottom waters, and the seafloor, collated from multiple sources (e.g., ref. [39–45]) (Table S1). Specifically, the surface-water data include temperature, primary productivity, current velocity, and ocean ecoregion division (cf. ref. [40]). The bottom-water data consist of temperature, primary productivity, current velocity, dissolved oxygen concentration, and salinity. The seafloor data include minimum distance to shore and

underwater spreading ridge systems, sedimentation rate, water depth, seafloor slope, benthic biomass, sediment total organic carbon (TOC), sediment porosity, and sediment type. These data principally represent environmental conditions but also include ecological (e.g., biomass, ecoregion division) and jointly environmental-ecological observations (e.g., productivity, TOC).

After spatially binning all target variable observations (Db and L) to 5-minute resolution (609 data points for Db and 505 for L) and correlating these target variables to georeferenced predictor variables (see "Methods"), we used a combination of 'unsupervised' and 'supervised' machine-learning techniques to explore their relationships and to make more highly resolved predictions of the distribution of Db and L values over the global ocean. For unsupervised machine learning, we used principal component analysis (PCA) to explore the relationship between each target variable (Db or L) and numerical predictor variables (environmental and ecological parameters), as well as the relationships between the numerical predictor variables. To quantitatively constrain the relationship between Db or L and these predictor variables, and to predict values of Db and L over the global ocean, we employed the Random Forest (RF) algorithm, a tree-based ensemble supervised machine-learning technique that offers low bias, moderate variance, and performs well in capturing non-linear relationships[46] (see "Methods"). We explored the relative contributions of each predictor variable to the predicted values of Db or L in a consistent and locally accurate manner by calculating SHAP (SHapley Additive exPlanations) values[47] for each parameter based on the trained RF model. We further employed our trained RF model to generate maps of the spatial variation in Db and L (as well as their standard errors) for the global ocean at a 5-minute spatial resolution, and estimated the extent to which marine protected areas (MPAs) foster the healthy operation of benthic ecological processes, including types of bioturbation that promote sediment mixing.

Results

Our comparative analyses indicate that, in contrast to common perception[21,23], no single dominant environmental or ecological parameter uniquely corresponds to either Db or L. In contrast, a range of parameters emerge that, either negatively or positively, correlate with these metrics of sediment mixing. Further, we find that the parameters that most strongly correlate with Db are, in many cases, not the same as those that most strongly correlate with L. This is important because previous studies have suggested that higher intensities of sediment mixing by benthic organisms promote greater mixed layer depths (e.g., ref. [20,22,48]), a framework that assumes that controls on Db and L are equivalent, although this is not always supported by field observations[20–22,49]. Analysis of the Db and L observations within our database indicate that, globally, Db ranges from 0.17 (25^{th} percentile) to 8.94 (75^{th} percentile) $cm^2\ yr^{-1}$ and L ranges from 3.8 (25^{th} percentile) to 9.0 (75^{th} percentile) cm (Figure 1; hereafter, all ranges represent 25^{th}–75^{th} percentiles, unless otherwise stated), giving an estimated global volume of actively bioturbated sediment of ~13,700–32,500 km^3 for a global seafloor area of ~361 million km^2. However, these observations also indicate contrasting levels of variability between the shelf (here, all marine settings landward of the shelf break[40]) and the open ocean: Db values are higher in shelf regions[40] (0.61–18.8 $cm^2\ yr^{-1}$) relative to the open ocean (0.05–1.0 $cm^2\ yr^{-1}$), whereas L values are similar across shelf (3.6–11.0 cm) and open-ocean (3.8–8.0 cm) regions. Assessment of these data using a Mann-Whitney U test further indicates that these differences in Db values between shelf and open-ocean settings are statistically significant (p-value < 2.2e-16) whereas differences in L values are not (p-value = 0.054). This distinction in spatial clustering between Db and L is also supported by Moran's I statistics (0.55 for Db and 0.38 for L), suggesting a more pronounced spatial clustering for Db compared to L.

Both Db and L display highly non-linear relationships with numerical environmental and ecological predictor variables (Figure S1), but a stronger correlation is observed between these variables and Db than between these variables and L (Figure S1). We observe that various predictor variables, including seafloor (benthic) biomass (across different trophic and size classes), primary productivity of bottom and surface waters, current velocity of bottom and surface waters, bottom-water temperature, sedimentation rate, seafloor sediment TOC, and distance to spreading ridge, show a significant positive correlation with Db (Figure S1). In contrast, water depth, bottom-water salinity, seafloor slope, seafloor sediment porosity, and distance to shore demonstrate a significant negative correlation with Db. The range of predictor variables that significantly correlate with L, however, is notably narrower (Figure S1). Significant positive correlations with L are limited to seafloor sediment TOC, seafloor macrofauna biomass, and bottom-water primary productivity; no significant negative relationships are evident.

To further explore correlations among numerical predictor variables and to facilitate the identification of a suitable parameter set for supervised machine learning, we computed the Variance Inflation Factor (VIF) for each predictor variable in the Db and L dataset (Figure S2A, B). The majority of variables exhibit relatively low VIF values (below 10), suggesting relatively low multicollinearity[50]. However, both seafloor macrofauna biomass and megafauna biomass demonstrate relatively high VIF values (>10), highlighting their substantial correlation with other parameters. To mitigate potential multicollinearity, we removed the biomass parameters before running the Random Forest machine-learning model (see below). The VIF values for all remaining parameters are below 10 (Figure S2C, D), indicating relatively low multicollinearity

and enhancing the reliability of the rankings of feature importance produced by machine learning.

Spearman's correlation analyses (Figure 2) assessing the relationship between the numerical predictor variables and each target variable reveal a more pronounced correlation between Db and the environmental and ecological parameters we consider (the ten largest absolute correlation coefficients are greater than 0.3) than emerges for L (all absolute correlation coefficients are less than 0.2). In agreement with some previous findings[20], the environmental and ecological parameters that have the highest degree of correlation with Db are distinct from those that have the highest degree of correlation with L (Figure 2). Of the ten most strongly correlated environmental and ecological predictor variables, seafloor (benthic) biomass (across various trophic and size classes), bottom- and surface-water primary productivity, bottom-water current velocity, and seafloor sediment TOC exhibit a strong positive correlation with Db, whereas seafloor macrofauna biomass, bottom-water dissolved oxygen, bottom-water primary productivity, bottom-water current velocity, seafloor megafauna biomass, and sedimentation rate are positively (but weakly) correlated with L (Figure 2). Similarly, water depth and distance to shore negatively correlate with Db, whereas seafloor sediment TOC, seafloor slope, and surface-water current velocity, albeit weakly, negatively correlate with L (Figure 2). A negative correlation between seafloor sediment TOC and L has been previously reported[26] but, notably, we find that the correlation coefficients for L are considerably weaker than those for Db. We also find variable degrees of interdependency between a range of environmental and ecological parameters (Figure S3).

Our PCA analysis (Figure 3) of numerical predictor variables reveals that seafloor biomass, bottom- and surface-water primary productivity, sedimentation rate, sediment TOC, and bottom-water temperature, each characterized by relatively higher PC1 values, can be grouped together and are associated with higher Db values (Figure 3A). Conversely, water depth, sediment porosity, distance to shore, and surface-water temperature, characterized by lower PC1 values, can be grouped together and are associated with lower Db values (Figure 3A). A similar grouping of predictor variables is observed for the dataset linked to L. However, similar L values occur in both the negative and positive PC1 fields of our predictor variables (Figure 3B), reflecting weak relationships between L and these environmental and ecological parameters. This disparity underscores the potentially strong variability in the extent to which environmental and ecological parameters shape Db and L. Beyond the scope of PCA, we also observe that Db is characterized by greater disparity, relative to L, between distinct sediment types, with higher Db values observed in areas of the seafloor dominated by siliciclastic sands, silts and clays and lower Db values observed in sediments dominated by biogenic calcareous oozes (Figure S4).

To predict the finer-scale distribution of variability in Db and L (beyond the resolution afforded by previously available empirical datasets), we built a machine-learning model by selecting an initial set of fifteen mainly environmental parameters as predictor variables (Table S1) (based on knowledge accrued during our correlation and unsupervised machine-learning analyses) and using Db and L as target variables; we consider this our baseline scenario. We employed a 10-fold cross-validation method[51] to evaluate the predictive capability of our machine-learning model on unseen data. We selected the Random Forest (RF) model for its robust handling of high-dimensional data with complex non-linear relationships and its better predictive accuracy for our dataset, as evidenced by its higher R^2 values compared to other machine-learning

algorithms (Table S2). Our RF model represents a significant advance in global-scale predictive capability for Db (the 10-fold cross-validation R^2 value is 0.54; Figure 4A) relative to previous prediction efforts (e.g., R^2 values of 0.22 in ref. [21] and 0.43 in ref. [23]). For L, we obtained a 10-fold cross-validation R^2 value of 0.29 (Figure 4B). Previous efforts to predict L vary widely, with R^2 values ranging from 0.001 in ref. [21] to 0.47 in ref. [26] or 0.88 in ref. [25], but these analyses did not have the same observation density, spatial coverage or spatial resolution as our dataset. Larger R^2 values for the prediction of L emergent from previous studies[25,26] suggest that smaller datasets do not adequately capture the global-scale heterogeneity of values and environmental correlates that emerges from our larger and more robustly validated (e.g., using 10-fold cross-validation) dataset. The relative importance of each variable, as determined by SHAP value (Figure 4C, D), indicates that the top five parameters that most strongly correlate with Db are water depth (negative correlation; Figure S5A–D), surface-water primary productivity (positive correlation), bottom-water primary productivity (positive correlation), sediment type (categorical variable, so no numerical correlation), and distance to shore (negative correlation). The top five parameters that most strongly correlate with L are sediment TOC (negative correlation; Figure S5E–I), surface-water primary productivity (positive correlation), water depth (negative correlation in shallower water and positive correlation in deeper water), bottom-water salinity (negative correlation), and distance to shore (negative correlation). It is notable that the mean |SHAP| values for all parameters, when predicting L, are substantially lower compared to those associated with prediction of Db, and thus lower confidence should be attributed to predictions of L from correlative environmental and ecological parameters (Figure 4C, D).

To examine the potential for enhancing model accuracy with more predictor variables, we incorporated additional ecological parameters into the RF model, including benthic biomass and

biogeographical ecoregion division. As RF predictions of Db and L using this more comprehensive set of global environmental and ecological parameters did not increase model fit (R^2 values: Db, 0.51; L, 0.26) relative to RF results using our smaller subset of variables, and given the risk of introducing more multicollinearity into the parameter space, we omitted these additional ecological parameters from subsequent machine-learning analyses. To examine the influence of sampling bias—stemming from the uneven distribution of Db and L observations across the seafloor (Figure 1; ref. [30])—on model accuracy and interpretation, we employed a randomized sub-sampling technique. Specifically, we randomly sampled 50% of the entire Db or L dataset, with the selection probability scaled by the inverse density of samples within each 10×10˚ grid, across the entire global seafloor (Figure S6A, C). This method markedly diminished sample clustering in particular regions, serving as a robust sensitivity analysis for evaluating model performance. Applying the RF model to these Db and L subsets and the corresponding subset of environmental and ecological parameters did not substantively change model outcomes (10-fold cross-validation R^2: Db, 0.55; L, 0.22) or the rank importance of predictive parameters (Db subset: water depth, followed by surface-water primary productivity, bottom-water primary productivity, and sediment type; L subset: sediment TOC followed by surface-water primary productivity) (Figure S6B, D). To investigate the potential for methodological differences in collection of bioturbation data to shape model outcomes—particularly given the disparate time scales of integration represented by different bioturbation proxies (e.g., common use of different radioisotope systems as well as particulate tracers and textural proxies, cf. ref. [30]), we subsampled all Db and L data originally derived from ^{210}Pb observations, which represent a substantial share of the whole dataset (62% for Db and 62% for L). We observe that even when constrained to a single (and shared) methodology, the disparity between Db and L persists.

Specifically, when using only the ^{210}Pb data, machine learning still performs better for Db (R^2 = 0.57) than for L (R^2 = 0.3), with R^2 values similar to those of our baseline scenario (R^2 = 0.54 for Db and 0.29 for L). Additionally, we find congruence in four of the top five most important features for Db, and four of the top five most important features for L, between the ^{210}Pb-based analyses and our baseline scenario (Figure S7; Figure 4C, D).

Next, to explore whether the environmental and ecological parameters vary in their relative importance in predicting variations in Db and L between different environmental settings, we independently trained RF models to predict Db and L in shelf and open-ocean regions. We find that the predictability either diminished or remained comparable relative to model performance using the full global ocean dataset (R^2: shelf Db = 0.40, L = 0.28; open-ocean Db = 0.44, L = 0.33). The ranking of environmental and ecological parameter importance for shelf Db aligns with findings emergent from the full dataset, with water depth, sediment type, bottom-water primary productivity, and surface-water primary productivity retaining their status as the parameters with the greatest predictive power (Figure 5A). Conversely, for open-ocean Db, surface-water primary productivity, distance to spreading ridge, surface-water current velocity, and sediment TOC emerge as the strongest environmental and ecological predictors, whereas water depth, distance to shore, and bottom-water productivity emerge as relatively unimportant (Figure 5C). For L, the environmental and ecological parameters with the highest predictive power in shelf and open-ocean settings are similar to those identified for the full dataset, with surface-water primary productivity, distance to shore, sediment TOC, and water depth emerging as the strongest environmental and ecological correlates in shelf settings (Figure 5B), and surface-water primary productivity, sediment TOC, bottom-water dissolved oxygen, and water depth holding the greatest predictive power in open-ocean settings (Figure 5D).

After applying the RF model (trained using the full dataset) to our selected suite of 15 environmental and ecological parameters across the global ocean, we generated high-resolution maps of predicted Db and L (and associated standard error) across the global seafloor (Figure 6). Because Random Forest learns and makes predictions based on the patterns and relationships found within the sample dataset, its performance can be limited when predicting conditions that significantly deviate from those encountered during training. The value range of the training predictor variables encompasses approximately 97–99% of the values of predictor variables across the global ocean, indicating that the trained RF model can derive robust global patterns with minimal extrapolation. These maps show that predicted Db values range from 0.12 to 0.50 $cm^2\ yr^{-1}$ and that L ranges from 5.6 to 8.7 cm (25^{th} and 75^{th} percentiles, respectively). Mirroring the broad-scale patterns that emerged from the empirical dataset, predicted Db values are higher in shelf settings (0.69–3.78 $cm^2\ yr^{-1}$) relative to open-ocean regions (0.11–0.30 $cm^2\ yr^{-1}$), whereas L values (shelf, 5.0–7.1 cm; open-ocean, 5.8–9.0 cm) do not show this dichotomy.

Utilizing our predicted global maps of Db and L, we assessed whether the implementation of marine protected areas (MPAs)[52], in general, promote higher levels of bioturbation and thus the healthy functioning of benthic ecological processes. By comparing values of Db and L within designated MPAs ("within MPA", Figure 7) with those determined for an equivalently sized and immediately adjacent non-protected area ("surrounding MPA", Figure 7), we find that values of Db and L within (Db: 3.1–9.7 $cm^2\ yr^{-1}$; L: 5.5–7.6 cm) and surrounding MPAs (Db: 2.5–9.4 $cm^2\ yr^{-1}$; L: 5.5–7.5 cm) are broadly comparable (Figure 7B, C). The relative percentage change for either Db or L between MPAs and surrounding areas is limited (Db, median change is 0.54% and -2.9%–6.3% for 25^{th} to 75^{th} percentile; L, median change is 0.11% and -1.2%–2.2% for 25^{th} to 75^{th} percentile; Figure 7B, C). Wilcoxon Signed-Rank analyses reject the null hypothesis of no

297 relative change, for both Db and L, between MPAs and surrounding areas (p = 1.5e-12 for Db
298 and 8e-9 for L), indicating a detectable albeit limited disparity between MPAs and surrounding
299 unprotected areas; median percent change values are nonetheless close to 0%. We also find that
300 the relative change (either positive or negative) between MPA and non-MPA pairs does not
301 appear to vary systematically with geographic location. To quantify the impact of machine-
302 learning uncertainty on these estimates of percentage change, we employed Monte Carlo
303 resampling (1000 iterations) to randomly sample both Db and L values for each pixel,
304 considering the standard error, and calculate the relative percentage change between MPAs and
305 unprotected surrounding areas. These analyses yield percentage changes ranging from -5.1% to
306 9.1% for Db (25^{th} and 75^{th} percentile, with a median of 1.1%) and from -2.8% to 4.1% for L
307 (with a median of 0.49%), further underscoring that most protection measures do not appear to
308 be sufficiently targeted to substantially impact bioturbation, as predicted by its environmental
309 and ecological correlates.

310 **Discussion**

311 Our unsupervised and supervised machine-learning models applied to the full global inventory of
312 Db and L highlight the variability inherent in each of these bioturbation metrics (and the
313 processes they represent). Therefore, when inferring underlying patterns in distribution—
314 whether local, regional or global—it is critical to consider the broadest possible representation of
315 bioturbation. Our analyses also strongly suggest that a wide range of environmental and
316 ecological factors[53]—and not individual factors such as sediment accumulation rate[21,54,55] or
317 water depth[23] alone—are strongly correlated with and may play a significant role in shaping
318 bioturbation intensity and sediment mixed layer depth on a global scale. The positive
319 multivariate relationships we have identified may indicate that bioturbation intensities and depths

are linked strongly to parameters relating directly to food supply and availability, productivity and benthic biodiversity, whereas the negative multivariate relationships may potentially reflect either changes in body size and other species traits with water depth[44,56] or reductions in surface-ocean or benthic productivity or export productivity associated with changes in nutrient or light availability[30,57] that coincide with increasing water depth or distance from land. However, the interdependencies between these variables (Figure S3) may hamper precise mechanistic evaluation, and it is important to emphasize that, within our identified subsets of correlates, the relative importance of specific abiotic and biotic variables are likely to vary with location, timing, environmental setting and ecology[35].

Given that several of the environmental and ecological parameters that emerge from our analyses as particularly strong correlates (and potential drivers) of bioturbation intensity have been proposed to have varied considerably across the Phanerozoic—most notably productivity and benthic biomass[58–60]—this suggests that Phanerozoic increases in productivity and benthic metabolic expenditure may have contributed to observed secular increases in bioturbation intensity, as previous studies have suggested (e.g., ref. [58,61–64]). Importantly, however, evolutionary changes in bioturbation intensity may not have translated into directional changes in sediment mixed layer depth. Although not environmentally invariant, as has previously been suggested[20], from our analyses L values do not appear to group strongly on the basis of either water depth or sedimentation rate, nor to be as readily predicted as Db by any correlative environmental and ecological parameters, whether alone or in combination (Figure 2B, 3B, 4) and regardless of proxy system employed (Figure S7). Although both Db and L are linked to the bioturbation activities of burrowing infauna[20,22,48], this disparity strongly suggests that environmental and ecological processes shaping intensities and depths of faunal-mediated

sediment mixing are likely decoupled. These findings emphasize the need for greater mechanistic understanding of the processes that influence the development and depth of the sediment mixed layer[25,53] and how these differ from processes that shape biodiffusion intensity. Previous studies have also noted disparities between environmental patterns of Db and L and have suggested that L may be limited by the high metabolic costs of burrowing deeper as sediments become increasingly compacted, and by the declining availability of labile organic matter[20,21]. However, we do not observe a strong correlation between L and either sediment type, porosity, or sedimentation rate (Figure 3, S3, S4), and recent work has highlighted that burrowing invertebrates adjust the mechanical efficiency of their burrowing behavior, allowing burrow networks and vertical mixing to extend to depths beyond expectations based on the physical properties of the sediment profile[65]. Similarly, bottom-water primary productivity and sediment TOC are strongly correlated with Db, but are notably weaker correlates of L. We conclude, therefore, that although the rheology and organic content of seafloor sediments may indeed influence styles and intensities of burrowing (and may have additionally shaped the Phanerozoic evolution of bioturbation depths and intensities, as previous studies have suggested; e.g., ref. [61–64,66]), they do not appear to sufficiently account for the variable distribution of mixed layer depths in the modern oceans.

The dichotomy we observe between patterns of correlation for Db and L may potentially reflect the inability of our compiled global environmental and ecological dataset to capture transient or rapid community responses to environmental variation. Both bioturbation and many of the environmental and ecological parameters represented in our dataset vary dramatically on seasonal or even shorter time scales[48,67–70], as well as along environmental gradients[71]. The inability of our model to more robustly predict L suggests that mixed layer depth may be

366 comparatively more varied, on relatively fine spatial or temporal scales, than mixing intensity. If
367 these observations hold true, this implies that Db may more closely track the behavioral and
368 functional diversity of the community (which, in turn, may be regulated by longer-term
369 environmental conditions), whereas L may be more sensitive to the impact of seasonally variable
370 local environmental conditions on the abundance and biomass of bioturbating fauna. We suggest
371 that coupled collection of bioturbation and environmental data at a higher temporal resolution
372 should be a priority for future studies. We cannot rule out, however, that variability in Db and/or
373 L may reflect other factors not yet determined at a global scale[19], in particular ecological
374 responses to change (e.g., intraspecific variability, dominance, composition, and
375 compensation)[36,72–74]. This underscores the potential vulnerability of seafloor level-bottom
376 communities to short-term climate and environmental perturbations; it is anticipated that
377 accelerating rates of not only coastal but also open-ocean and deep-water warming[75] will affect
378 species' behavior[35,76], and reductions in seafloor biomass associated with climate change[16,17] will
379 minimize benthic community contributions. Further, the non-linear relationships we observe
380 between our environmental and ecological predictor variables and Db and L (Figure S1) suggest
381 a heightened risk that abrupt fundamental shifts in processes critical to benthic functioning, such
382 as bioturbation, will occur as environmental thresholds are crossed under climate forcing[77,78], as
383 has already begun in regions of climate amplification[71].

384 The diminished significance of water depth and bottom-water primary productivity in predicting
385 open-ocean Db, as opposed to shelf Db (Figure 5), may reflect the inherent heterogeneity (and
386 more productive nature) of shallow-water seafloor systems. In shelf settings, water depth (and
387 associated hydrodynamic energy) varies considerably relative to seafloor area and appears to be
388 associated with substantial variability in Db. In contrast, in open-ocean settings, the association

between water depth and Db is comparatively weak. Bioturbation intensities in open-ocean settings may, therefore, be comparatively less responsive, respond on longer timescales, or be 'buffered' against the effects of environmental variability.

Despite our model's global scale, its high resolution (5-minute pixels) enables the identification of smaller-scale patterns. Our findings on the relationship between MPAs and bioturbation suggest that management of benthic resources to promote seafloor ecosystem health may be insufficiently targeted across a variety of geographic and environmental settings, presumably because protection measures are commonly not tailored to seafloor biodiversity and functioning and do not comprehensively protect the seafloor from all salient critical pressures[79–82]. If we are to mitigate the effects of anthropogenic activity and climate change on seafloor functioning, better understanding will likely be essential to more robustly evaluate when and how the contributions of bioturbating species are compromised[83], how altered biodiversity[8] and post-perturbation compensatory mechanisms alter biodiversity-ecosystem function relations[17,73], and how the ecology of benthic environments can deliver transformative change to enhance and deliver innovative adaptation plans[84,85].

Acknowledgments

We thank N. Planavsky, C. Ma and M. Zhao for useful discussions that shaped this research. We also thank S. van de Velde and two anonymous reviewers for their detailed and insightful comments that helped improve the manuscript. M. S. acknowledges grant NE/K001906/1 from Natural Environment Research Council, and L. T. acknowledges support from Yale University. The authors acknowledge support from the Yale Center for Research Computing. Portions of this

research were conducted with the advanced computing resources provided by Texas A&M High Performance Research Computing.

Author contributions

S.Z., L.T., and M.S. designed research; S.Z., M.S., and L.T. provided methodology; S.Z. performed research, analyzed data, and contributed new modeling tools; S.Z., L.T., and M.S. wrote the paper.

Declaration of interests

The authors declare no competing interests.

Figures Legends

Figure 1. Spatial distribution of bioturbation intensity (Db) and sediment mixed layer depth (L) values over the global ocean. (A) The spatial distribution of $\log_{10}$(Db) (n = 609). (B) The spatial distribution of $\log_{10}$(L) (n = 505). In each display panel, points represent spatially binned information at a spatial resolution of 5 × 5 minutes. The insets display histogram distributions of Db and L, with data for each bioturbation metric split into 30 equal bins.

Figure 2. Spearman's rank correlation coefficient between bioturbation and the environmental and ecological parameters. (A) Bioturbation intensity (Db). (B) Sediment mixed layer depth (L). Red bars indicate a positive correlation, whereas blue bars signify a negative correlation. The absolute value of the correlation coefficient decreases from top to bottom of each diagram. See also Figure S1, S2 and S3.

Figure 3. Projection of the environmental and ecological parameters on the first and second principal components. Observations are shown as points in the plane formed by two principal

components (PC1 and PC2) and are colored according to values of (A) bioturbation intensity (Db) or (B) sediment mixed layer depth (L). The arrows represent the PCA loadings of the environmental and ecological parameters. See also Figure S4.

Figure 4. Machine-learning (Random Forest model) outcomes for bioturbation intensity (Db) and sediment mixed layer depth (L). The correspondence between predicted and observed values of (A) Db and (B) L values are shown for the 10-fold hold-out test dataset (data unseen during the training stage). The red line represents a hypothetical 1:1 correspondence. (C, D) The mean absolute SHAP values (displayed in decreasing order, from top to bottom) associated with calculation of target variables (Db and L) from predictor variables (i.e., environmental and ecological parameters). See also Figure S5, S6, and S7.

Figure 5. Machine-learning outcomes for Db and L for samples located in the shelf region and in the open-ocean region. (A, B) The mean absolute SHAP associated with calculation of target variables Db and L from predictor variables in the shelf region. (C, D) The mean absolute SHAP associated with calculation of target variables Db and L from predictor variables in the open-ocean region.

Figure 6. Random Forest-generated predictions of the global distribution of modern marine bioturbation intensity (Db) and sediment mixed layer depth (L). (A, C) Predicted value at 5-minute resolution by the Random Forest model from geospatially correlative environmental and ecological variables. (B, D) Standard error of the predicted value at 5-minute resolution. Marine white regions represent areas lacking predictor variable data.

Figure 7. Comparison of predicted Db and L values between marine protected areas (MPAs) and equivalent adjacent non-protected areas. (A) Locations of each of the 5056 marine protected areas (red polygons) alongside the area-equivalent adjacent non-protected areas (blue polygons). (B, C) distribution of the predicted mean bioturbation intensity (Db) and predicted mean sediment mixed layer depth (L) for each marine protected area and the equivalent adjacent non-protected area, for the subset of MPAs exceeding 2 pixels in size. Insets indicate the distribution of percentage change of predicted mean bioturbation intensity (Db) or predicted mean sediment mixed layer depth (L) values between each marine protected area and the paired equivalent and adjacent non-protected area. Note that extreme percentage change values (the uppermost 0.5% and lowermost 0.5%) are omitted from the insets of panels B and C for clarity.

STAR Methods

RESOURCE AVAILABILITY

Lead contact

Further information and requests for resources and reagents should be directed to and will be fulfilled by the lead contact, Shuang Zhang (shuang-zhang@tamu.edu).

Materials availability

No unique reagents were generated in this study.

Data and code availability

All raw and spatially binned Db and L data needed to evaluate the conclusions in the paper are present in the Supplemental Information. The raw Db and L data are also available at https://doi.org/10.7910/DVN/GBELFW. The code used to analyze the data, run the machine-learning model, and produce the global Db and L maps, as well as additional supporting information, have been posted to the Zenodo platform (https://zenodo.org/records/11069160).

METHOD DETAILS

Establishing a dataset of global patterns in bioturbation

We utilized a recently published fully georeferenced compilation of marine bioturbation data which includes reported values of the biodiffusion intensity coefficient (Db, $cm^2\ yr^{-1}$) and the depth of the sediment mixed layer (L, cm) as published in peer-reviewed literature[30]. This bioturbation dataset was meticulously compiled to exclude areas disturbed by human activities, particularly those subjected to extensive trawling. As this dataset encompasses a wide range of methods for measuring Db and L that demonstrate methodological dependency[27,85–89], we constrained our analysis to data obtained using downcore profiles of radioisotopes, chlorophyll *a*, and particulate tracers, such as luminophores and tek beads (for both Db and L); glass beads (Db only); organic carbon, luminescence and x-ray profiles, as well as values calculated from modeling of geochemical profile data (L only). These data were further processed by averaging intra-locality data (georeferenced to the same latitude and longitude) through time for individual localities. As both the Db and L data are right-skewed, we applied a $\log_{10}$ transformation to mitigate the skewness, stabilize the variance, and reduce any impact of outliers (Figure 1). To reduce the impact of outliers on our analyses we then removed the lowermost and uppermost 1% of observations from each of these two bioturbation datasets. To match point measurements of

493 Db and L with associated environmental and ecological parameters, we binned our Db and L
494 data to a spatial resolution of 5 × 5 arc minutes. Specifically, multiple data points within 5 arc
495 minutes were averaged. The final dataset contains 609 values for Db and 505 values for L.
496
497 **Linking Db and L to spatially correlative environmental and ecological data**
498 We assessed the relationship between Db or L values and a range of marine environmental and
499 ecological parameters from the same georeferenced areas. These parameters (for data resolution
500 and sources, see Table S1) include surface ocean features (including ocean ecoregion division,
501 surface-water temperature, surface-water primary productivity, and surface current velocity);
502 bottom-water features (including bottom-water temperature, bottom-water primary productivity,
503 bottom-water current velocity, bottom-water dissolved oxygen concentration, and bottom-water
504 salinity); and seafloor features (including minimum distances to shore and underwater spreading
505 ridge systems, sedimentation rate, water depth, seafloor slope, benthic biomass, sedimentary total
506 organic carbon (TOC), sediment porosity, and sediment type).
507
508 To account for differences in environmental conditions, we determined 15 divisions (in a
509 shapefile vector format) from Bailey's ecoregions of the oceans[40]: Shelf, Equatorial
510 Countercurrent Division, Equatorial Trades Division, Trade Winds Division, Poleward Trades
511 Division, High-Salinity Tropical Monsoon Division, Tropical Monsoon Division, Poleward
512 Monsoon Division, Jet Stream Division, High-Salinity Subtropical Division, Subtropical
513 Division, Equatorial Westerlies Division, Poleward Westerlies Division, Outer Polar Division,
514 and Inner Polar Division. For seafloor sediment type, data were converted to a shapefile vector
515 format (from the original raster format) and are comprised of 13 sediment types[41], including

gravel and coarser, sand, silt, clay, ash and volcanic sand/gravel, fine-grained calcareous sediment, siliceous mud, calcareous ooze, radiolarian ooze, diatom ooze, sponge spicules, mixed calcareous-siliceous ooze, and shells and coral fragments. Ecoregion division and sediment type are both categorical variables. To associate Db and L values with categorical values for each ecoregion division and seafloor sediment type, we calculated the distance between each Db or L pixel and different divisions and sediment types and then determined the nearest division and sediment type and assigned those to each Db or L pixel. The geospatial analyses described above were accomplished using GRASS GIS[90] and R[91].

Principal component analysis (PCA)

We conducted the PCA analysis on the numerical predictor variables in R using the PCA() function from the FactoMineR package[92]. The arrows in Figure 3 represent the PCA loadings of the environmental and ecological parameters. The length of each arrow indicates the strength of correlation between each environmental and ecological parameter and the principal components: a longer arrow signifies a stronger correlation with the principal components, whereas a shorter arrow signifies a weaker correlation. Each arrow's direction reflects the relationship between that parameter and the axes, indicating that the parameter positively or negatively influences the principal components. Accordingly, parameters represented by arrows pointing in similar directions are positively correlated with each other, whereas those pointing in opposite directions are negatively correlated with each other. Parameters represented by arrows that are perpendicular to one another are not correlated.

Supervised machine learning

To quantitatively predict and map Db and L over the global ocean, we employed the Random Forest (RF) algorithm[46]. RF is based on a decision tree, which is a non-parametric supervised learning algorithm used for classification or regression and that captures non-linear relationships in the data and is robust to input outliers[93]. However, decision trees can also be prone to overfitting (i.e., high variance), be relatively low in predictive accuracy and may not yield optimal solutions. RF can be thought of as an ensemble of many trees (the 'bagging' technique), thereby reducing the high variance experienced by a single decision tree. Unlike simple bagging, RF further decorrelates the trees, using a random set of predictor variables to divide the training data during each split. All these modifications contribute to the high predictive accuracy (low bias and moderate variance) of RF. The RF algorithm has been widely used in geoscience research[94,95] and is particularly suited, as here, to making predictions using high-dimensional data with complex non-linear relationships (Figure S1). The construction of the RF model was conducted in R[91] using the "range" package[96]. Optimal values of hyperparameters (i.e., number of trees and minimum node size) in the RF model were generated by implementing a 10-fold cross-validation coupled with a grid search in the training process. Specifically, we employed a random partitioning strategy to divide the entire dataset into 10 subsets. We set aside one of these subsets for evaluation purposes (i.e., the hold-out dataset), while we used the remaining nine subsets to train the model. We assessed model performance across a range of number of trees (from 500 to 1500) and conducted sensitivity analyses of minimum node size, ranging from 1 to 10. Mean-squared-error (MSE) was used as an indicator of performance. The tuned parameters that yield the smallest average MSE of the hold-out test data (i.e., test set in the 10-fold cross-validation) were selected as the best parameters. We then used the best set of hyperparameters to train our RF model on the entire dataset to generate the final model.

562 Compared with linear models, the RF model excels at capturing non-linear relationships between
563 variables and identifying complex patterns that linear models may overlook. We performed the
564 same task with a range of different machine-learning algorithms to independently verify the
565 suitability of applying RF to our dataset; the lower R^2 values for Db and L emergent from other
566 algorithms (Table S2) confirms the appropriateness of our selection of the RF algorithm.
567 Moreover, the consistent disparity in predictive power between Db and L across various
568 algorithms supports the robustness of our interpretations regarding the challenges associated with
569 using environmental and ecological parameters to predict L relative to Db (see Table S2 for
570 details about these algorithms). The uncertainty (standard error) of the RF model was quantified
571 using the Infinitesimal Jackknife method[97], which is particularly useful for complex machine-
572 learning models (such as the RF model) where traditional resampling-based methods may be
573 computationally prohibitive. When applied to the RF model, the Infinitesimal Jackknife works
574 by calculating the infinitesimal perturbations of each individual tree with respect to the data on
575 which it was trained. These perturbations are then aggregated to provide an overall estimate of
576 the standard error of the model's predictions (see Figure 6 for the standard error when mapping
577 Db and L over the global seafloor).
578
579 To illustrate the relative contributions of each predictor variable to the predicted Db or L values,
580 we calculated the SHAP value for each variable based on the final model. SHAP ("SHapley
581 Additive exPlanations") values represent the importance of each individual variable for tree
582 ensembles in a consistent and locally accurate manner[47]. The fundamental principle of SHAP is
583 based on random permutation. However, unlike the simple permutation method (i.e., permuting
584 one column and comparing the prediction generated from this permuted dataset with the original

prediction), the SHAP method calculates the contributions of each parameter by averaging the differences in predictions across every possible parameter ordering. This approach considers interactions between parameters and compares the contributions of parameters fairly. In particular, the interpretation of the SHAP value for parameter *x* in one sample represents the contribution of parameter *x* to the prediction of this specific sample compared to the average prediction for the entire dataset. A positive SHAP value for a specific *x* indicates that the current *x* value contributes positively to the difference between the prediction of the specific focal sample and the average of the entire dataset. The correlation between the SHAP value of *x* and the *x* value itself signifies the relationship between the *x* variable and the target variable. A positive trend indicates a positive correlation, while a negative trend indicates a negative correlation. The mean |SHAP| value of parameter *x* for all samples represents the overall absolute contribution of *x* to the prediction, which is treated as the feature importance for *x* (Figure 4).

To further test the impact of multicollinearity among predictor variables on the model's ability to rank feature importance, we implemented a scenario with an even smaller set of predictor variables than our baseline. In this refined scenario, we removed bottom-water primary productivity and distance to shore, each of which exhibits high correlation with water depth, from the parameter space. Negligible improvement in VIF metrics was observed for this smaller dataset compared with the baseline scenario. The most important predictors for Db and L that emerged from this analysis align closely with our baseline results, reinforcing the validity of the feature importance ranking of our baseline scenario.

Effectiveness of marine protected areas

We compiled marine protected area (MPA) information from the shapefile in the World Database on Protected Areas[52]. MPAs were selected by choosing the rows that had "designated" values for the "STATUS" field and "100% marine PA" for the "MARINE" field in the shapefile. We also unified MPA rows that had the same MPA name, resulting in 5056 MPA multi-polygons. To generate an area-equivalent adjacent non-protected region for each MPA, we first calculated the centroid for each MPA, then gradually enlarged a buffer polygon surrounding the centroid until the difference in area between the buffer and the MPA polygon was equivalent to the area of the MPA. After subtracting each MPA polygon from its buffer polygon, we obtained the area-equivalent adjacent polygon (Figure 7A). The area ratio of the non-protected region to the MPA region ranges from 0.9 to 1.1, supporting a direct comparison of the Db and L values between each pair of MPA regions and the non-MPA regions.

We overlaid each MPA region and its adjacent non-protected region on the predicted global Db and L maps and extracted the mean Db and L values. Given the pixel resolution of the predicted global Db and L values at 5 minutes by 5 minutes, certain small MPA regions and non-MPA regions may fall within the same pixel. This situation can bias comparisons, as the granularity of a single pixel is insufficient to discern meaningful differences between MPAs and non-MPA regions. To mitigate this potential bias, we applied a filter to include only MPA regions comprising at least three pixels, yielding a refined dataset of 1,534 MPA regions for further analysis. The distribution of Db and L values show similar magnitudes between the screened MPA regions and their adjacent regions (Figure 7B, C). To further compare the Db and L values in MPA regions versus adjacent non-protected regions, we calculated the Log Response Ratio (LRR):

$$LRR = \log\left(\frac{Mean\ Db\ or\ L\ in\ MPA}{Mean\ Db\ or\ L\ in\ adjacent\ region}\right)$$

In a final step, we calculated the relative percentage change of Db or L ($\%\ Change = 100\% \times (e^{LRR} - 1)$; Figure 7B, C).

QUANTIFICATION AND STATISTICAL ANALYSIS

We conducted the Mann-Whitney U test for the Db and L values between shelf and open-ocean settings. We calculated Moran's I statistics for the Db and L values. We future conducted Wilcoxon Signed-Rank test for the relative change of Db and L values from areas immediately surrounding each MPA to the MPA.

Supplementary Dataset files

Data S1: Raw Db and L data used for analysis in this study.

Data S2: Geographically binned Db data (5-min resolution).

Data S3: Geographically binned L data (5-min resolution).

References

1. Middelburg, J.J. (2018). Reviews and syntheses: To the bottom of carbon processing at the seafloor. Biogeosciences *15*, 413–427. https://doi.org/10.5194/bg-15-413-2018.

2. Snelgrove, P.V.R., Soetaert, K., Solan, M., Thrush, S., Wei, C.-L., Danovaro, R., Fulweiler, R.W., Kitazato, H., Ingole, B., Norkko, A., et al. (2018). Global carbon cycling on a heterogeneous seafloor. Trends Ecol. Evol. *33*, 96–105. 10.1016/j.tree.2017.11.004.

3. Van Cappellen, P., and Ingall, E.D. (1996). Redox stabilization of the atmosphere and oceans by phosphorus-limited marine productivity. Science *271*, 493–496. 10.1126/science.271.5248.493.

4. Isson, T.T., Planavsky, N.J., Coogan, L.A., Stewart, E.M., Ague, J.J., Bolton, E.W., Zhang, S., McKenzie, N.R., and Kump, L.R. (2020). Evolution of the Global Carbon Cycle and Climate Regulation on Earth. Glob. Biogeochem. Cycles *34*, 2018GB006061. 10.1029/2018GB006061.

5. Aller, R.C. (1982). The effects of macrobenthos on chemical properties of marine sediment and overlying water. In Animal-Sediment Relations: The Biogenic Alteration of Sediments Topics in Geobiology., P. L. McCall and M. J. S. Tevesz, eds. (Springer US), pp. 53–102. 10.1007/978-1-4757-1317-6_2.

6. Meysman, F.J.R., Middelburg, J.J., and Heip, C.H.R. (2006). Bioturbation: A fresh look at Darwin's last idea. Trends Ecol. Evol. *21*, 688–695. 10.1016/j.tree.2006.08.002.

7. Rhoads, D.C., and Young, D.K. (1970). The influence of deposit-feeding organisms on sediment stability and community structure. J Mar Res *28*, 150–178.

8. Solan, M., Cardinale, B.J., Downing, A.L., Engelhardt, K.A.M., Ruesink, J.L., and Srivastava, D.S. (2004). Extinction and ecosystem function in the marine benthos. Science *306*, 1177–1180. 10.1126/science.1103960.

9. Boyle, R.A., Dahl, T.W., Dale, A.W., Shields-Zhou, G.A., Zhu, M., Brasier, M.D., Canfield, D.E., and Lenton, T.M. (2014). Stabilization of the coupled oxygen and phosphorus cycles by the evolution of bioturbation. Nat. Geosci. *7*, 671–676. 10.1038/ngeo2213.

10. Tarhan, L.G., Zhao, M., and Planavsky, N.J. (2021). Bioturbation feedbacks on the phosphorus cycle. Earth Planet. Sci. Lett. *566*, 116961. 10.1016/j.epsl.2021.116961.

11. Dale, A.W., Boyle, R.A., Lenton, T.M., Ingall, E.D., and Wallmann, K. (2016). A model for microbial phosphorus cycling in bioturbated marine sediments: Significance for phosphorus burial in the early Paleozoic. Geochim. Cosmochim. Acta *189*, 251–268. 10.1016/j.gca.2016.05.046.

12. van de Velde, S.J., Dale, A.W., and Arndt, S. (2023). Bioturbation and the δ56Fe signature of dissolved iron fluxes from marine sediments. R. Soc. Open Sci. *10*, 220010. 10.1098/rsos.220010.

13. van de Velde, S., Mills, B.J.W., Meysman, F.J.R., Lenton, T.M., and Poulton, S.W. (2018). Early Palaeozoic ocean anoxia and global warming driven by the evolution of shallow burrowing. Nat. Commun. *9*, 2554. 10.1038/s41467-018-04973-4.

14. Danovaro, R., Gambi, C., Dell'Anno, A., Corinaldesi, C., Fraschetti, S., Vanreusel, A., Vincx, M., and Gooday, A.J. (2008). Exponential decline of deep-sea ecosystem functioning linked to benthic biodiversity loss. Curr. Biol. *18*, 1–8. 10.1016/j.cub.2007.11.056.

15. Worm, B., Barbier, E.B., Beaumont, N., Duffy, J.E., Folke, C., Halpern, B.S., Jackson, J.B.C., Lotze, H.K., Micheli, F., Palumbi, S.R., et al. (2006). Impacts of biodiversity loss on ocean ecosystem services. Science *314*, 787–790. 10.1126/science.1132294.

16. Jones, D.O.B., Yool, A., Wei, C.-L., Henson, S.A., Ruhl, H.A., Watson, R.A., and Gehlen, M. (2014). Global reductions in seafloor biomass in response to climate change. Glob. Change Biol. *20*, 1861–1872. 10.1111/gcb.12480.

17. Sweetman, A.K., Thurber, A.R., Smith, C.R., Levin, L.A., Mora, C., Wei, C.-L., Gooday, A.J., Jones, D.O.B., Rex, M., Yasuhara, M., et al. (2017). Major impacts of climate change on deep-sea benthic ecosystems. Elem. Sci. Anthr. *5*, 4. 10.1525/elementa.203.

18. Yool, A., Martin, A.P., Anderson, T.R., Bett, B.J., Jones, D.O.B., and Ruhl, H.A. (2017). Big in the benthos: Future change of seafloor community biomass in a global, body size-resolved model. Glob. Change Biol. *23*, 3554–3566. 10.1111/gcb.13680.

19. Schmidt-Traub, G. (2021). National climate and biodiversity strategies are hamstrung by a lack of maps. Nat. Ecol. Evol. *5*, 1325–1327. 10.1038/s41559-021-01533-w.

20. Boudreau, B.P. (1998). Mean mixed depth of sediments: The wherefore and the why. Limnol. Oceanogr. *43*, 524–526. 10.4319/lo.1998.43.3.0524.

21. Boudreau, B.P. (1994). Is burial velocity a master parameter for bioturbation? Geochim. Cosmochim. Acta *58*, 1243–1249. 10.1016/0016-7037(94)90378-6.

22. Jumars, P.A., and Wheatcroft, R.A. (1989). Responses of benthos to changing food quality and quantity, with a focus on deposit feeding and bioturbation. In Productivity of the Ocean: Present and Past (Wiley), pp. 235–253.

23. Middelburg, J.J., Soetaert, K., and Herman, P.M.J. (1997). Empirical relationships for use in global diagenetic models. Deep Sea Res. Part Oceanogr. Res. Pap. *44*, 327–344. 10.1016/S0967-0637(96)00101-X.

24. Smith, C.R., Berelson, W., Demaster, D.J., Dobbs, F.C., Hammond, D., Hoover, D.J., Pope, R.H., and Stephens, M. (1997). Latitudinal variations in benthic processes in the abyssal equatorial Pacific: control by biogenic particle flux. Deep Sea Res. Part II Top. Stud. Oceanogr. *44*, 2295–2317. 10.1016/S0967-0645(97)00022-2.

25. Smith, C.R., and Rabouille, C. (2002). What controls the mixed-layer depth in deep-sea sediments? The importance of POC flux. Limnol. Oceanogr. *47*, 418–426. 10.4319/lo.2002.47.2.0418.

26. Song, S., Santos, I.R., Yu, H., Wang, F., Burnett, W.C., Bianchi, T.S., Dong, J., Lian, E., Zhao, B., Mayer, L., et al. (2022). A global assessment of the mixed layer in coastal sediments and implications for carbon storage. Nat. Commun. *13*, 4903. 10.1038/s41467-022-32650-0.

27. Teal, L.R., Bulling, M.T., Parker, E.R., and Solan, M. (2008). Global patterns of bioturbation intensity and mixed depth of marine soft sediments. Aquat. Biol. *2*, 207–218. 10.3354/ab00052.

28. Weinert, M., Kröncke, I., Meyer, J., Mathis, M., Pohlmann, T., and Reiss, H. (2022). Benthic ecosystem functioning under climate change: modelling the bioturbation potential for benthic key species in the southern North Sea. PeerJ *10*, e14105. 10.7717/peerj.14105.

29. Hohmann, N. (2022). Global compilation of surface mixed layer parameters (sedimentation rate, bioturbation depth, mixing intensity) from marine environments: The SMLBase v1.0. Front. Earth Sci. *10*.

30. Solan, M., Ward, E.R., White, E.L., Hibberd, E.E., Cassidy, C., Schuster, J.M., Hale, R., and Godbold, J.A. (2019). Worldwide measurements of bioturbation intensity, ventilation rate, and the mixing depth of marine sediments. Sci. Data *6*, 1–6. 10.1038/s41597-019-0069-7.

31. Bernard, G., Gammal, J., Järnström, M., Norkko, J., and Norkko, A. (2019). Quantifying bioturbation across coastal seascapes: Habitat characteristics modify effects of macrofaunal communities. J. Sea Res. *152*, 101766. 10.1016/j.seares.2019.101766.

32. Gogina, M., Zettler, M.L., Vanaverbeke, J., Dannheim, J., Van Hoey, G., Desroy, N., Wrede, A., Reiss, H., Degraer, S., Van Lancker, V., et al. (2020). Interregional comparison of benthic ecosystem functioning: Community bioturbation potential in four regions along the NE Atlantic shelf. Ecol. Indic. *110*, 105945. 10.1016/j.ecolind.2019.105945.

33. Emmerson, M.C., Solan, M., Emes, C., Paterson, D.M., and Raffaelli, D. (2001). Consistent patterns and the idiosyncratic effects of biodiversity in marine ecosystems. Nature *411*, 73–77. 10.1038/35075055.

34. Godbold, J.A., Bulling, M.T., and Solan, M. (2011). Habitat structure mediates biodiversity effects on ecosystem properties. Proc. R. Soc. B Biol. Sci. *278*, 2510–2518. 10.1098/rspb.2010.2414.

35. Godbold, J.A., and Solan, M. (2009). Relative importance of biodiversity and the abiotic environment in mediating an ecosystem process. Mar. Ecol. Prog. Ser. *396*, 273–282.

36. Wohlgemuth, D., Solan, M., and Godbold, J.A. (2017). Species contributions to ecosystem process and function can be population dependent and modified by biotic and abiotic setting. Proc. R. Soc. B Biol. Sci. *284*, 20162805. 10.1098/rspb.2016.2805.

37. Bernardino, P.N., De Keersmaecker, W., Fensholt, R., Verbesselt, J., Somers, B., and Horion, S. (2020). Global-scale characterization of turning points in arid and semi-arid ecosystem functioning. Glob. Ecol. Biogeogr. *29*, 1230–1245. 10.1111/geb.13099.

38. Donovan, M.K., Burkepile, D.E., Kratochwill, C., Shlesinger, T., Sully, S., Oliver, T.A., Hodgson, G., Freiwald, J., and van Woesik, R. (2021). Local conditions magnify coral loss after marine heatwaves. Science *372*, 977–980. 10.1126/science.abd9464.

39. Assis, J., Tyberghein, L., Bosch, S., Verbruggen, H., Serrão, E.A., and Clerck, O.D. (2018). Bio-ORACLE v2.0: Extending marine data layers for bioclimatic modelling. Glob. Ecol. Biogeogr. *27*, 277–284. 10.1111/geb.12693.

40. Bailey, R.G. (2014). Ecoregions: The ecosystem geography of the oceans and continents 2nd ed. 2014 edition. (Springer).

41. Dutkiewicz, A., Müller, R.D., O'Callaghan, S., and Jónasson, H. (2015). Census of seafloor sediments in the world's ocean. Geology *43*, 795–798. 10.1130/G36883.1.

42. Lee, T.R., Wood, W.T., and Phrampus, B.J. (2019). A machine learning (KNN) approach to predicting global seafloor total organic carbon. Glob. Biogeochem. Cycles *33*, 37–46. 10.1029/2018GB005992.

43. Martin, K.M., Wood, W.T., and Becker, J.J. (2015). A global prediction of seafloor sediment porosity using machine learning. Geophys. Res. Lett. *42*, 10640–10646. 10.1002/2015GL065279.

44. Wei, C.-L., Rowe, G.T., Escobar-Briones, E., Boetius, A., Soltwedel, T., Caley, M.J., Soliman, Y., Huettmann, F., Qu, F., Yu, Z., et al. (2010). Global patterns and predictions of seafloor biomass using Random Forests. PLOS ONE *5*, e15323. 10.1371/journal.pone.0015323.

45. Halevy, I., Fike, D.A., Pasquier, V., Bryant, R.N., Wenk, C.B., Turchyn, A.V., Johnston, D.T., and Claypool, G.E. (2023). Sedimentary parameters control the sulfur isotope composition of marine pyrite. Science *382*, 946–951. 10.1126/science.adh1215.

46. Breiman, L. (2001). Random Forests. Mach. Lang. *45*, 5–32. 10.1023/A:1010933404324.

47. Lundberg, S., and Lee, S.-I. (2017). A unified approach to interpreting model predictions. ArXiv170507874 Cs Stat.

48. Smith, C.R. (1992). Factors Controlling Bioturbation in Deep-Sea Sediments and Their Relation to Models of Carbon Diagenesis. In Deep-Sea Food Chains and the Global Carbon Cycle NATO ASI Series., G. T. Rowe and V. Pariente, eds. (Springer Netherlands), pp. 375–393. 10.1007/978-94-011-2452-2_23.

49. Smith, C.R., A. Levin, L., Hoover, D.J., McMurtry, G., and Gage, J.D. (2000). Variations in bioturbation across the oxygen minimum zone in the northwest Arabian Sea. Deep Sea Res. Part II Top. Stud. Oceanogr. *47*, 227–257. 10.1016/S0967-0645(99)00108-3.

50. James, G., Witten, D., Hastie, T., and Tibshirani, R. (2017). An Introduction to Statistical Learning: with Applications in R 1st ed. 2013, Corr. 7th printing 2017 edition. (Springer).

51. Graw, J.H., Wood, W.T., and Phrampus, B.J. (2023). Predicting Marine In Situ Heat Flow Using a Geospatial Machine Learning Conformal Prediction. Geochem. Geophys. Geosystems *24*, e2023GC010913. 10.1029/2023GC010913.

52. UNEP-WCMC (2020). Protected planet: The world database on protected areas (WDPA)/the global database on protected areas management effectiveness (GD-PAME) [on-line]. UNEP-WCMC Camb. UK Available Wwwprotectedplanetnet.

53. Teal, L.R., Parker, E.R., and Solan, M. (2010). Sediment mixed layer as a proxy for benthic ecosystem process and function. Mar. Ecol. Prog. Ser. *414*, 27–40. 10.3354/meps08736.

54. Tromp, T.K., Van Cappellen, P., and Key, R.M. (1995). A global model for the early diagenesis of organic carbon and organic phosphorus in marine sediments. Geochim. Cosmochim. Acta *59*, 1259–1284. 10.1016/0016-7037(95)00042-X.

55. Van Cappellen, P., Gaillard, J.-F., and Rabouille, C. (1993). Biogeochemical transformations in sediments: Kinetic models of early diagenesis. In Interactions of C, N, P and S Biogeochemical Cycles and Global Change NATO ASI Series., R. Wollast, F. T. Mackenzie, and L. Chou, eds. (Springer), pp. 401–445. 10.1007/978-3-642-76064-8_17.

56. Stratmann, T., van Oevelen, D., Martínez Arbizu, P., Wei, C.-L., Liao, J.-X., Cusson, M., Scrosati, R.A., Archambault, P., Snelgrove, P.V.R., Ramey-Balci, P.A., et al. (2020). The BenBioDen database, a global database for meio-, macro- and megabenthic biomass and densities. Sci. Data *7*, 206. 10.1038/s41597-020-0551-2.

57. Dunne, J.P., Sarmiento, J.L., and Gnanadesikan, A. (2007). A synthesis of global particle export from the surface ocean and cycling through the ocean interior and on the seafloor. Glob. Biogeochem. Cycles *21*. 10.1029/2006GB002907.

58. Bambach, R.K. (1993). Seafood through time: Changes in biomass, energetics, and productivity in the marine ecosystem. Paleobiology *19*, 372–397.

59. Finnegan, S., McClain, C.M., Kosnik, M.A., and Payne, J.L. (2011). Escargots through time: An energetic comparison of marine gastropod assemblages before and after the Mesozoic Marine Revolution. Paleobiology *37*, 252–269. 10.1666/09066.1.

60. Vermeij, G.J. (2019). The efficiency paradox: How wasteful competitors forge thrifty ecosystems. Proc. Natl. Acad. Sci. *116*, 17619–17623. 10.1073/pnas.1901785116.

61. Tarhan, L.G. (2018). The early Paleozoic development of bioturbation—Evolutionary and geobiological consequences. Earth-Sci. Rev. *178*, 177–207. 10.1016/j.earscirev.2018.01.011.

62. Thayer, C.W. (1979). Biological bulldozers and the evolution of marine benthic communities. Science *203*, 458–461. 10.1126/science.203.4379.458.

63. Larson, D.W., and Rhoads, D.C. (1983). The Evolution of Infaunal Communities and Sedimentary Fabrics. In Biotic Interactions in Recent and Fossil Benthic Communities Topics in Geobiology., M. J. S. Tevesz and P. L. McCall, eds. (Springer US), pp. 627–648. 10.1007/978-1-4757-0740-3_12.

64. Vermeij, G.J. (2013). On Escalation. Annu. Rev. Earth Planet. Sci. *41*, 1–19. 10.1146/annurev-earth-050212-124123.

65. Dorgan, K.M., Jumars, P.A., Johnson, B., Boudreau, B.P., and Landis, E. (2005). Burrow extension by crack propagation. Nature *433*, 475–475. 10.1038/433475a.

66. Tarhan, L.G. (2018). Phanerozoic shallow marine sole marks and substrate evolution. Geology *46*, 755–758. 10.1130/G45055.1.

67. Bernhardt, J.R., O'Connor, M.I., Sunday, J.M., and Gonzalez, A. (2020). Life in fluctuating environments. Philos. Trans. R. Soc. B Biol. Sci. *375*, 20190454. 10.1098/rstb.2019.0454.

68. Bulling, M.T., Hicks, N., Murray, L., Paterson, D.M., Raffaelli, D., White, P.C.L., and Solan, M. (2010). Marine biodiversity–ecosystem functions under uncertain environmental futures. Philos. Trans. R. Soc. B Biol. Sci. *365*, 2107–2116. 10.1098/rstb.2010.0022.

69. Solan, M., and Kennedy, R. (2002). Observation and quantification of in situ animal-sediment relations using time-lapse sediment profile imagery (t-SPI). Mar. Ecol. Prog. Ser. *228*, 179–191. 10.3354/meps228179.

70. Witte, U., Wenzhöfer, F., Sommer, S., Boetius, A., Heinz, P., Aberle, N., Sand, M., Cremer, A., Abraham, W.-R., Jørgensen, B.B., et al. (2003). In situ experimental evidence of the fate of a phytodetritus pulse at the abyssal sea floor. Nature *424*, 763–766. 10.1038/nature01799.

71. Solan, M., Ward, E.R., Wood, C.L., Reed, A.J., Grange, L.J., and Godbold, J.A. (2020). Climate-driven benthic invertebrate activity and biogeochemical functioning across the Barents Sea polar front. Philos. Trans. R. Soc. Math. Phys. Eng. Sci. *378*, 20190365. 10.1098/rsta.2019.0365.

72. Sanders, T., Solan, M., and Godbold, J.A. (2024). Trait-mediated processes and per capita contributions to ecosystem functioning depend on conspecific density and climate conditions. Commun. Earth Environ. *5*, 1–10. 10.1038/s43247-024-01237-6.

73. Thomsen, M.S., Garcia, C., Bolam, S.G., Parker, R., Godbold, J.A., and Solan, M. (2017). Consequences of biodiversity loss diverge from expectation due to post-extinction compensatory responses. Sci. Rep. *7*, 43695. 10.1038/srep43695.

74. Thomsen, M.S., Godbold, J.A., Garcia, C., Bolam, S.G., Parker, R., and Solan, M. (2019). Compensatory responses can alter the form of the biodiversity–function relation curve. Proc. R. Soc. B Biol. Sci. *286*, 20190287. 10.1098/rspb.2019.0287.

75. Brito-Morales, I., Schoeman, D.S., Molinos, J.G., Burrows, M.T., Klein, C.J., Arafeh-Dalmau, N., Kaschner, K., Garilao, C., Kesner-Reyes, K., and Richardson, A.J. (2020). Climate velocity reveals increasing exposure of deep-ocean biodiversity to future warming. Nat. Clim. Change *10*, 576–581. 10.1038/s41558-020-0773-5.

76. Bianchi, T.S., Brown, C.J., Snelgrove, P.V.R., Stanley, R.R.E., Cote, D., and Morris, C. (2023). Benthic Invertebrates on the Move: A Tale of Ocean Warming and Sediment Carbon Storage. Limnol. Oceanogr. Bull. *32*, 1–5. 10.1002/lob.10544.

77. Levin, L.A., Ekau, W., Gooday, A.J., Jorissen, F., Middelburg, J.J., Naqvi, S.W.A., Neira, C., Rabalais, N.N., and Zhang, J. (2009). Effects of natural and human-induced hypoxia on coastal benthos. Biogeosciences *6*, 2063–2098. 10.5194/bg-6-2063-2009.

78. Sahade, R., Lagger, C., Torre, L., Momo, F., Monien, P., Schloss, I., Barnes, D.K.A., Servetto, N., Tarantelli, S., Tatián, M., et al. (2015). Climate change and glacier retreat drive shifts in an Antarctic benthic ecosystem. Sci. Adv. *1*, e1500050. 10.1126/sciadv.1500050.

79. Allison, G.W., Lubchenco, J., and Carr, M.H. (1998). Marine reserves are necessary but not sufficient for marine conservation. Ecol. Appl. *8*, S79–S92. 10.2307/2641365.

80. Greathead, C., Magni, P., Vanaverbeke, J., Buhl-Mortensen, L., Janas, U., Blomqvist, M., Craeymeersch, J.A., Dannheim, J., Darr, A., Degraer, S., et al. (2020). A generic framework to assess the representation and

protection of benthic ecosystems in European marine protected areas. Aquat. Conserv. Mar. Freshw. Ecosyst. *30*, 1253–1275. 10.1002/aqc.3401.

81. Botterell, Z.L.R., Ribeiro, F., Alarcón-Ruales, D., Alfaro, E., Alfaro-Shigueto, J., Allan, N., Becerra, N., Braunholtz, L., Cardenas-Diaz, S., de Veer, D., et al. (2024). Plastic pollution transcends marine protected area boundaries in the eastern tropical and south-eastern Pacific. Mar. Pollut. Bull. *201*, 116271. 10.1016/j.marpolbul.2024.116271.

82. Filbee-Dexter, K., Starko, S., Pessarrodona, A., Wood, G., Norderhaug, K.M., Piñeiro-Corbeira, C., and Wernberg, T. Marine protected areas can be useful but are not a silver bullet for kelp conservation. J. Phycol. *n/a*. 10.1111/jpy.13446.

83. Garcia, C., Solan, M., Bolam, S.G., Sivyer, D., Parker, R., and Godbold, J.A. (2021). Exploration of multiple post-extinction compensatory scenarios improves the likelihood of determining the most realistic ecosystem future. Environ. Res. Commun. *3*, 045001. 10.1088/2515-7620/abf468.

84. Jackson, S.T. (2021). Transformational ecology and climate change. Science *373*, 1085–1086. 10.1126/science.abj6777.

85. Solan, M., Bennett, E.M., Mumby, P.J., Leyland, J., and Godbold, J.A. (2020). Benthic-based contributions to climate change mitigation and adaptation. Philos. Trans. R. Soc. B Biol. Sci. *375*, 20190107. 10.1098/rstb.2019.0107.

86. Gerino, M., Aller, R.C., Lee, C., Cochran, J.K., Aller, J.Y., Green, M.A., and Hirschberg, D. (1998). Comparison of different tracers and methods used to quantify bioturbation during a spring bloom: 234-Thorium, luminophores and chlorophylla. Estuar. Coast. Shelf Sci. *46*, 531–547. 10.1006/ecss.1997.0298.

87. Lecroart, P., Maire, O., Schmidt, S., Grémare, A., Anschutz, P., and Meysman, F.J.R. (2010). Bioturbation, short-lived radioisotopes, and the tracer-dependence of biodiffusion coefficients. Geochim. Cosmochim. Acta *74*, 6049–6063. 10.1016/j.gca.2010.06.010.

88. Smith, C.R., Pope, R.H., DeMaster, D.J., and Magaard, L. (1993). Age-dependent mixing of deep-sea sediments. Geochim. Cosmochim. Acta *57*, 1473–1488. 10.1016/0016-7037(93)90007-J.

89. Wheatcroft, R.A. (1992). Experimental tests for particle size-dependent bioturbation in the deep ocean. Limnol. Oceanogr. *37*, 90–104. 10.4319/lo.1992.37.1.0090.

90. GRASS Development Team (2017). Geographic Resources Analysis Support System (GRASS GIS) Software, Version 7.2 (Open Source Geospatial Foundation).

91. R Core Team (2017). R: A language and environment for statistical computing. R Found. Stat. Comput. Vienna Austria HttpswwwR-Proj.

92. Lê, S., Josse, J., and Husson, F. (2008). FactoMineR: An R Package for Multivariate Analysis. J. Stat. Softw. *25*, 1–18. 10.18637/jss.v025.i01.

93. Hastie, T., Tibshirani, R., and Friedman, J. (2016). The elements of statistical learning: Data mining, inference, and prediction, second edition 2nd edition. (Springer).

94. Carranza, C., Nolet, C., Pezij, M., and van der Ploeg, M. (2021). Root zone soil moisture estimation with Random Forest. J. Hydrol. *593*, 125840. 10.1016/j.jhydrol.2020.125840.

95. E, B., Zhang, S., Driscoll, C.T., and Wen, T. (2023). Human and natural impacts on the U.S. freshwater salinization and alkalinization: A machine learning approach. Sci. Total Environ. *889*, 164138. 10.1016/j.scitotenv.2023.164138.

96. Wright, M.N., and Ziegler, A. (2017). ranger: A Fast Implementation of Random Forests for High Dimensional Data in C++ and R. J. Stat. Softw. *77*, 1–17. 10.18637/jss.v077.i01.

97. Wager, S., Hastie, T., and Efron, B. (2014). Confidence Intervals for Random Forests: The Jackknife and the Infinitesimal Jackknife. J. Mach. Learn. Res. JMLR *15*, 1625–1651.

CellPress

TABLE FOR AUTHOR TO COMPLETE

Please do not add custom subheadings. *If you wish to make an entry that does not fall into one of the subheadings below, please contact your handling editor or add it under the "other"* subheading. ***Any subheadings not relevant to your study can be skipped.*** *(**NOTE:** references should be in numbered style, e.g., Smith et al.[1])*

Key resources table

REAGENT or RESOURCE	SOURCE	IDENTIFIER
Antibodies		
Bacterial and virus strains		
Biological samples		
Chemicals, peptides, and recombinant proteins		
Critical commercial assays		
Deposited data		
Raw Db and L data	Solan et al.[30]	https://dataverse.harvard.edu/dataset.xhtml?persistentId=doi:10.7910/DVN/GBELFW
Spatially binned Db and L data	This paper	N/A
Mean surface-water temperature	Assis et al.[39]	https://www.bio-oracle.org/downloads-to-email-v2.php?version=2_1

Mean surface current velocity	Assis et al.[39]	https://www.bio-oracle.org/downloads-to-email-v2.php?version=2_1
Mean bottom-water temperature	Assis et al.[39]	https://www.bio-oracle.org/downloads-to-email-v2.php?version=2_1
Mean bottom current velocity	Assis et al.[39]	https://www.bio-oracle.org/downloads-to-email-v2.php?version=2_1
Mean bottom-water salinity	Assis et al.[39]	https://www.bio-oracle.org/downloads-to-email-v2.php?version=2_1
Mean bottom-water dissolved oxygen concentration	Assis et al.[39]	https://www.bio-oracle.org/downloads-to-email-v2.php?version=2_1
Mean surface-water primary productivity	Assis et al.[39]	https://www.bio-oracle.org/downloads-to-email-v2.php?version=2_1
Mean bottom-water primary productivity	Assis et al.[39]	https://www.bio-oracle.org/downloads-to-email-v2.php?version=2_1
Water depth	Assis et al.[39]	https://www.bio-oracle.org/downloads-to-email-v2.php?version=2_1
Seafloor slope	Assis et al.[39]	https://www.bio-oracle.org/downloads-to-email-v2.php?version=2_1
Minimum distance to shoreline	Assis et al.[39]	https://www.bio-oracle.org/downloads-to-email-v2.php?version=2_1
Ocean ecoregion	Bailey[40]	https://link.springer.com/book/10.1007/978-1-4939-0524-9
Seafloor sediment type	Dutkiewicz et al.[41]	http://portal.gplates.org/portal/seafloor/
Seafloor sediment TOC content	Lee et al.[42]	https://zenodo.org/records/1471639
Seafloor sediment porosity	Martin et al.[43]	https://agupubs.onlinelibrary.wiley.com/doi/full/10.1002/2015GL065279
Ocean benthic biomass	Wei et al.[44]	https://journals.plos.org/plosone/article?id=10.1371/journal.pone.0015323

Sedimentation rate	Halevy et al.[45]	https://www.science.org/doi/10.1126/science.adh1215
Experimental models: Cell lines		
Experimental models: Organisms/strains		
Oligonucleotides		
Recombinant DNA		
Software and algorithms		
GRASS GIS v7.8	GRASS Development Team[90]	https://grass.osgeo.org
R v4.3.3	R Core Team[91]	https://www.r-project.org/
FactoMineR v2.8	Lê et al.[92]	https://cran.r-project.org/web/packages/FactoMineR
Ranger v0.15.1	Wright and Ziegler[96]	https://cran.r-project.org/web/packages/ranger
Other		

Figure

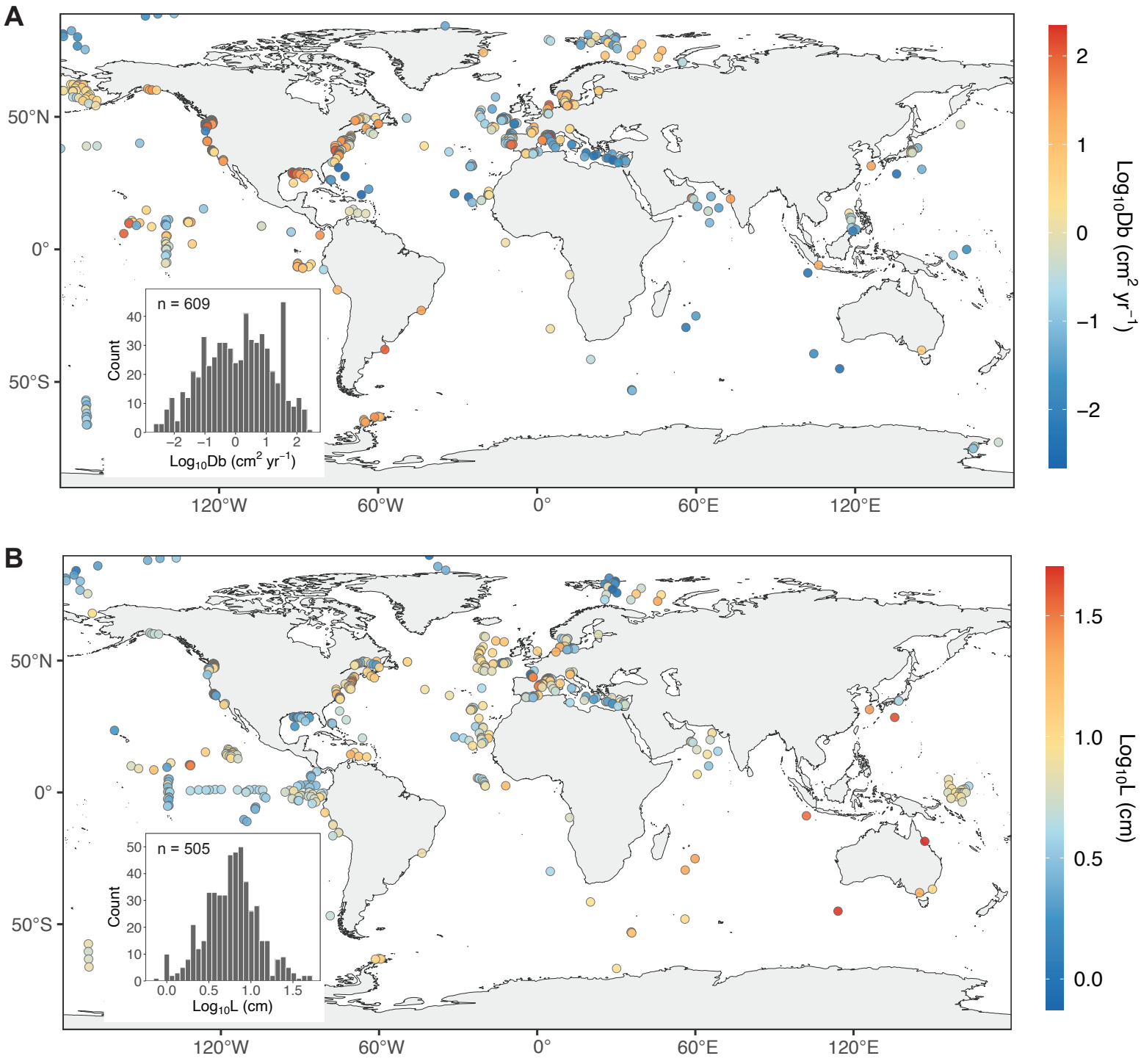
A
50°N
0°
50°S
120°W
60°W
0°
60°E
120°E
n = 609
Count
Log10Db (cm2 yr−1)
Log10Db (cm2 yr−1)
B
n = 505
Log10L (cm)
Log10L (cm)

Figure

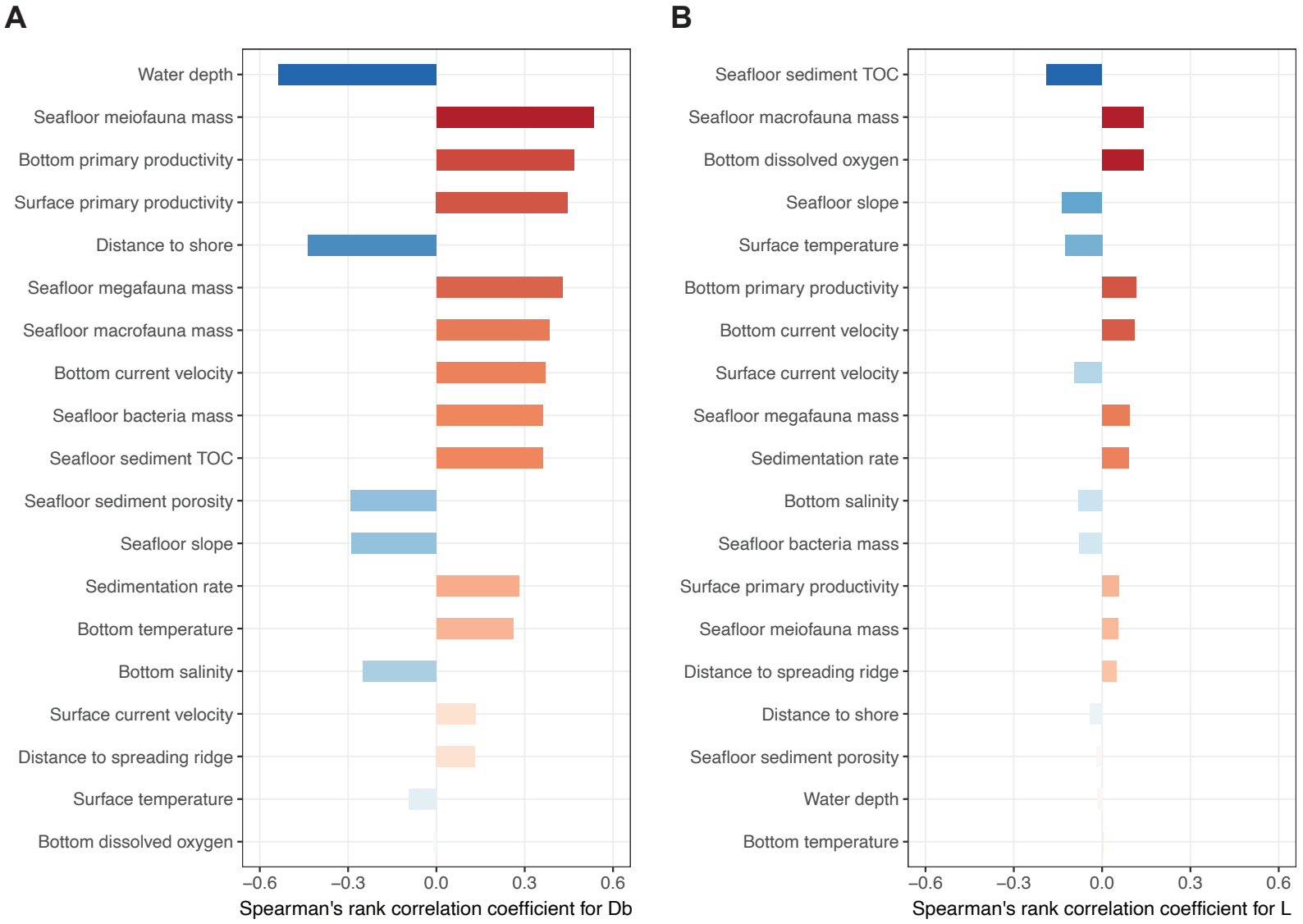
A
Water depth
Seafloor meiofauna mass
Bottom primary productivity
Surface primary productivity
Distance to shore
Seafloor megafauna mass
Seafloor macrofauna mass
Bottom current velocity
Seafloor bacteria mass
Seafloor sediment TOC
Seafloor sediment porosity
Seafloor slope
Sedimentation rate
Bottom temperature
Bottom salinity
Surface current velocity
Distance to spreading ridge
Surface temperature
Bottom dissolved oxygen
−0.6
−0.3
0.0
0.3
0.6
Spearman's rank correlation coefficient for Db
B
Seafloor sediment TOC
Seafloor macrofauna mass
Bottom dissolved oxygen
Seafloor slope
Surface temperature
Bottom primary productivity
Bottom current velocity
Surface current velocity
Seafloor megafauna mass
Sedimentation rate
Bottom salinity
Seafloor bacteria mass
Surface primary productivity
Seafloor meiofauna mass
Distance to spreading ridge
Distance to shore
Seafloor sediment porosity
Water depth
Bottom temperature
−0.6
−0.3
0.0
0.3
0.6
Spearman's rank correlation coefficient for L

Figure

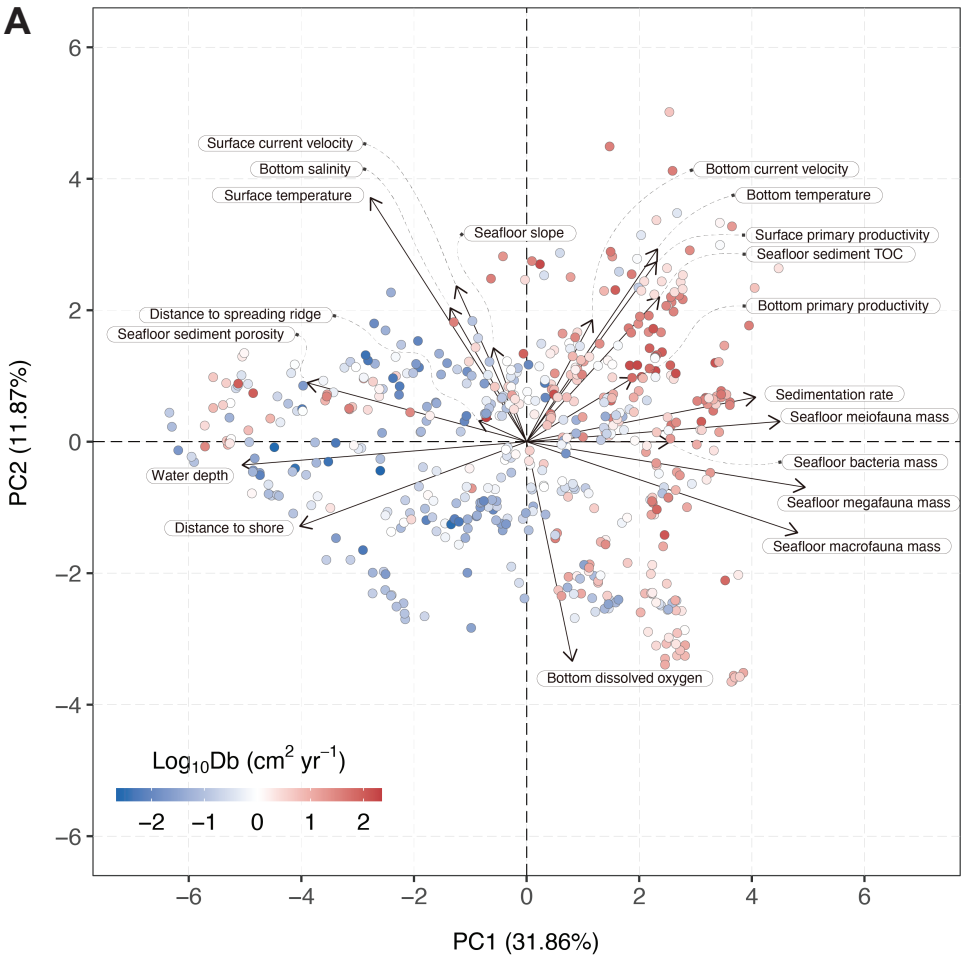
A
Surface current velocity
Bottom salinity
Surface temperature
Seafloor slope
Bottom current velocity
Bottom temperature
Surface primary productivity
Seafloor sediment TOC
Bottom primary productivity
Distance to spreading ridge
Seafloor sediment porosity
Sedimentation rate
Seafloor meiofauna mass
Seafloor bacteria mass
Water depth
Seafloor megafauna mass
Distance to shore
Seafloor macrofauna mass
Bottom dissolved oxygen
Log10Db (cm2 yr−1)
−2 −1 0 1 2
PC2 (11.87%)
PC1 (31.86%)

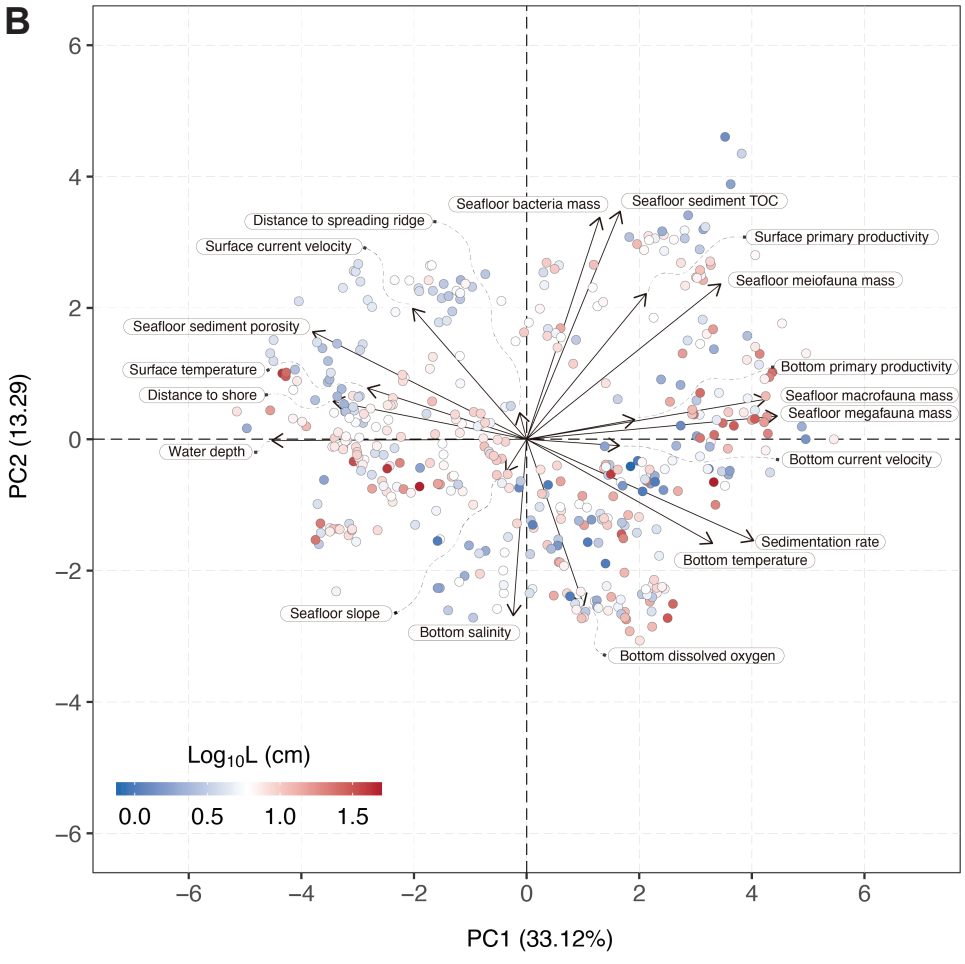
B
Seafloor bacteria mass
Seafloor sediment TOC
Distance to spreading ridge
Surface primary productivity
Surface current velocity
Seafloor meiofauna mass
Seafloor sediment porosity
Bottom primary productivity
Surface temperature
Seafloor macrofauna mass
Distance to shore
Seafloor megafauna mass
Water depth
Bottom current velocity
Sedimentation rate
Bottom temperature
Seafloor slope
Bottom salinity
Bottom dissolved oxygen
Log10L (cm)
0.0 0.5 1.0 1.5
PC2 (13.29)
PC1 (33.12%)

Figure

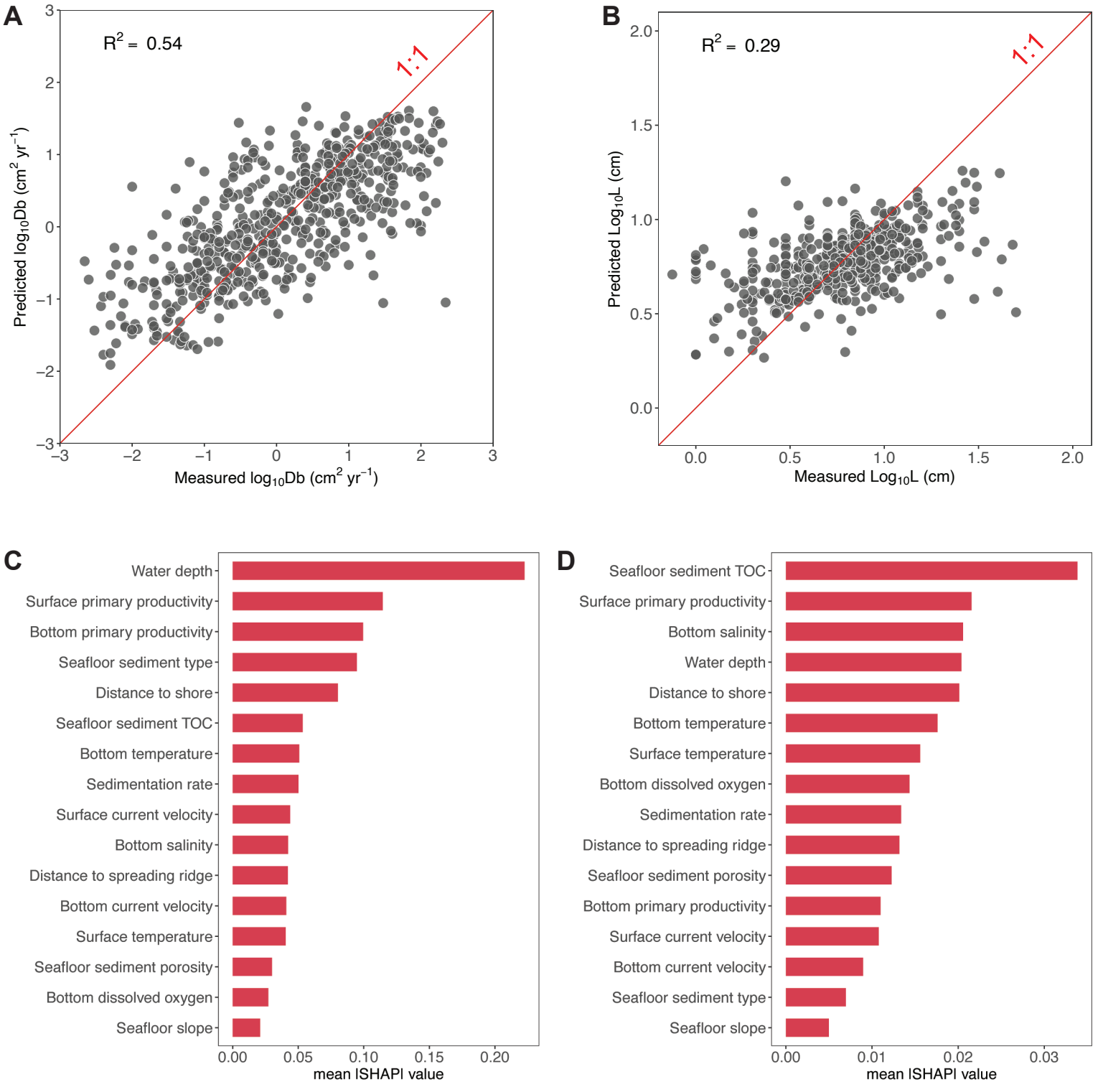
A
R^2 = 0.54
1:1
Predicted log_{10}Db (cm^2 yr^{-1})
Measured log_{10}Db (cm^2 yr^{-1})
B
R^2 = 0.29
1:1
Predicted Log_{10}L (cm)
Measured Log_{10}L (cm)
C
Water depth
Surface primary productivity
Bottom primary productivity
Seafloor sediment type
Distance to shore
Seafloor sediment TOC
Bottom temperature
Sedimentation rate
Surface current velocity
Bottom salinity
Distance to spreading ridge
Bottom current velocity
Surface temperature
Seafloor sediment porosity
Bottom dissolved oxygen
Seafloor slope
mean ISHAPI value
D
Seafloor sediment TOC
Surface primary productivity
Bottom salinity
Water depth
Distance to shore
Bottom temperature
Surface temperature
Bottom dissolved oxygen
Sedimentation rate
Distance to spreading ridge
Seafloor sediment porosity
Bottom primary productivity
Surface current velocity
Bottom current velocity
Seafloor sediment type
Seafloor slope
mean ISHAPI value

Figure

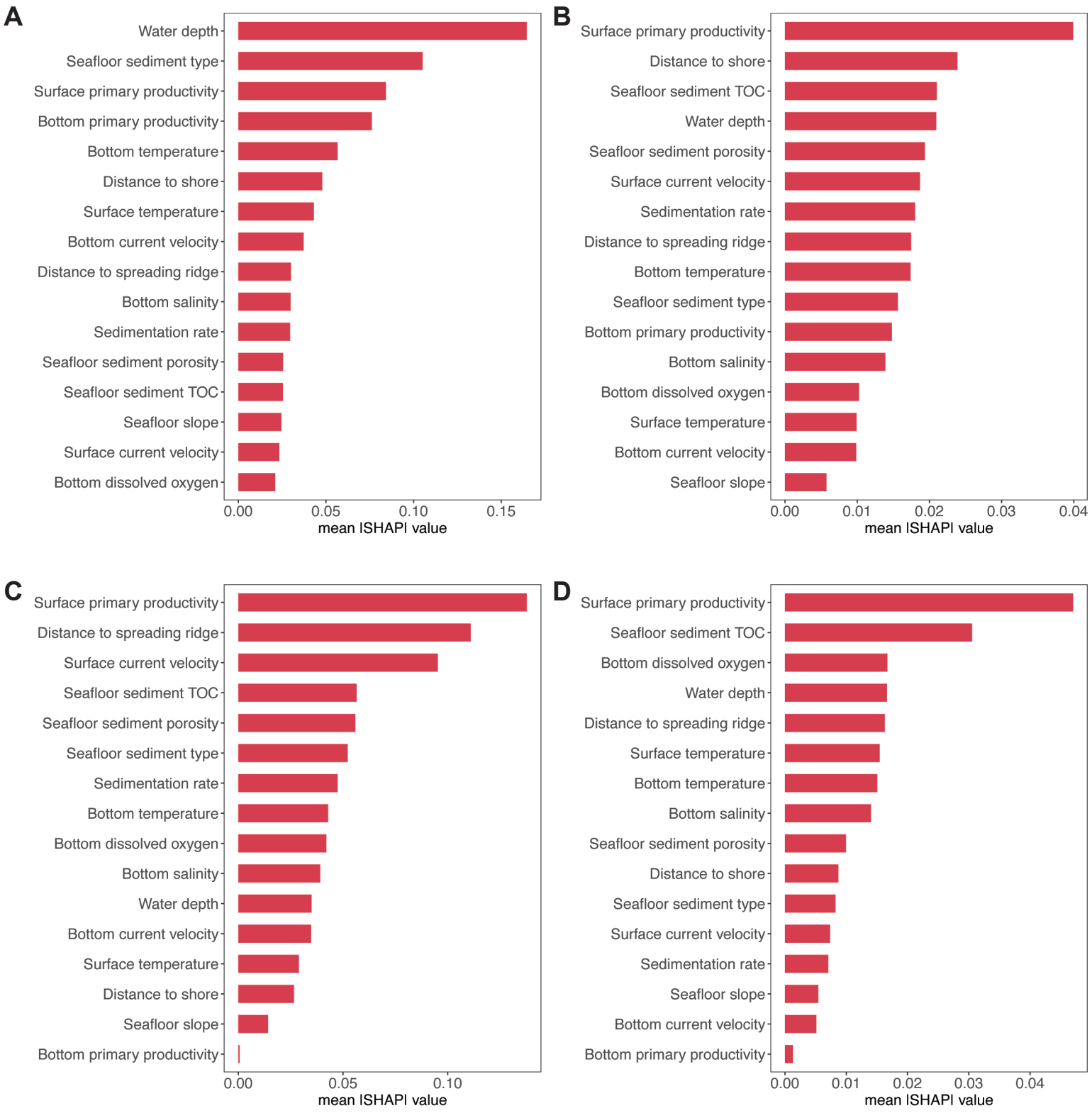
A
Water depth
Seafloor sediment type
Surface primary productivity
Bottom primary productivity
Bottom temperature
Distance to shore
Surface temperature
Bottom current velocity
Distance to spreading ridge
Bottom salinity
Sedimentation rate
Seafloor sediment porosity
Seafloor sediment TOC
Seafloor slope
Surface current velocity
Bottom dissolved oxygen
0.00
0.05
0.10
0.15
mean |SHAP| value
B
Surface primary productivity
Distance to shore
Seafloor sediment TOC
Water depth
Seafloor sediment porosity
Surface current velocity
Sedimentation rate
Distance to spreading ridge
Bottom temperature
Seafloor sediment type
Bottom primary productivity
Bottom salinity
Bottom dissolved oxygen
Surface temperature
Bottom current velocity
Seafloor slope
0.00
0.01
0.02
0.03
0.04
mean |SHAP| value
C
Surface primary productivity
Distance to spreading ridge
Surface current velocity
Seafloor sediment TOC
Seafloor sediment porosity
Seafloor sediment type
Sedimentation rate
Bottom temperature
Bottom dissolved oxygen
Bottom salinity
Water depth
Bottom current velocity
Surface temperature
Distance to shore
Seafloor slope
Bottom primary productivity
0.00
0.05
0.10
mean |SHAP| value
D
Surface primary productivity
Seafloor sediment TOC
Bottom dissolved oxygen
Water depth
Distance to spreading ridge
Surface temperature
Bottom temperature
Bottom salinity
Seafloor sediment porosity
Distance to shore
Seafloor sediment type
Surface current velocity
Sedimentation rate
Seafloor slope
Bottom current velocity
Bottom primary productivity
0.00
0.01
0.02
0.03
0.04
mean |SHAP| value

Figure

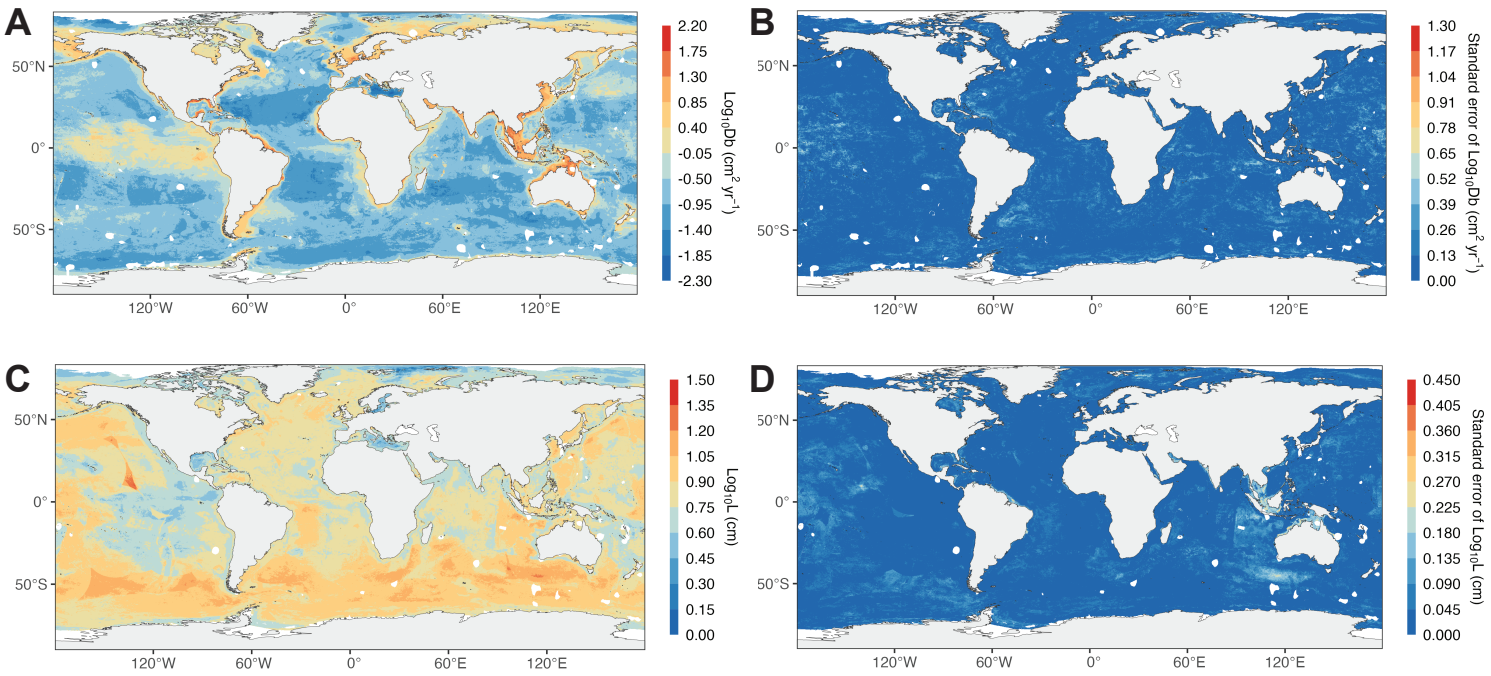
A
50°N
0°
50°S
120°W
60°W
0°
60°E
120°E
2.20
1.75
1.30
0.85
0.40
-0.05
-0.50
-0.95
-1.40
-1.85
-2.30
Log10Db (cm2 yr-1)
B
50°N
0°
50°S
120°W
60°W
0°
60°E
120°E
1.30
1.17
1.04
0.91
0.78
0.65
0.52
0.39
0.26
0.13
0.00
Standard error of Log10Db (cm2 yr-1)
C
50°N
0°
50°S
120°W
60°W
0°
60°E
120°E
1.50
1.35
1.20
1.05
0.90
0.75
0.60
0.45
0.30
0.15
0.00
Log10L (cm)
D
50°N
0°
50°S
120°W
60°W
0°
60°E
120°E
0.450
0.405
0.360
0.315
0.270
0.225
0.180
0.135
0.090
0.045
0.000
Standard error of Log10L (cm)

Figure

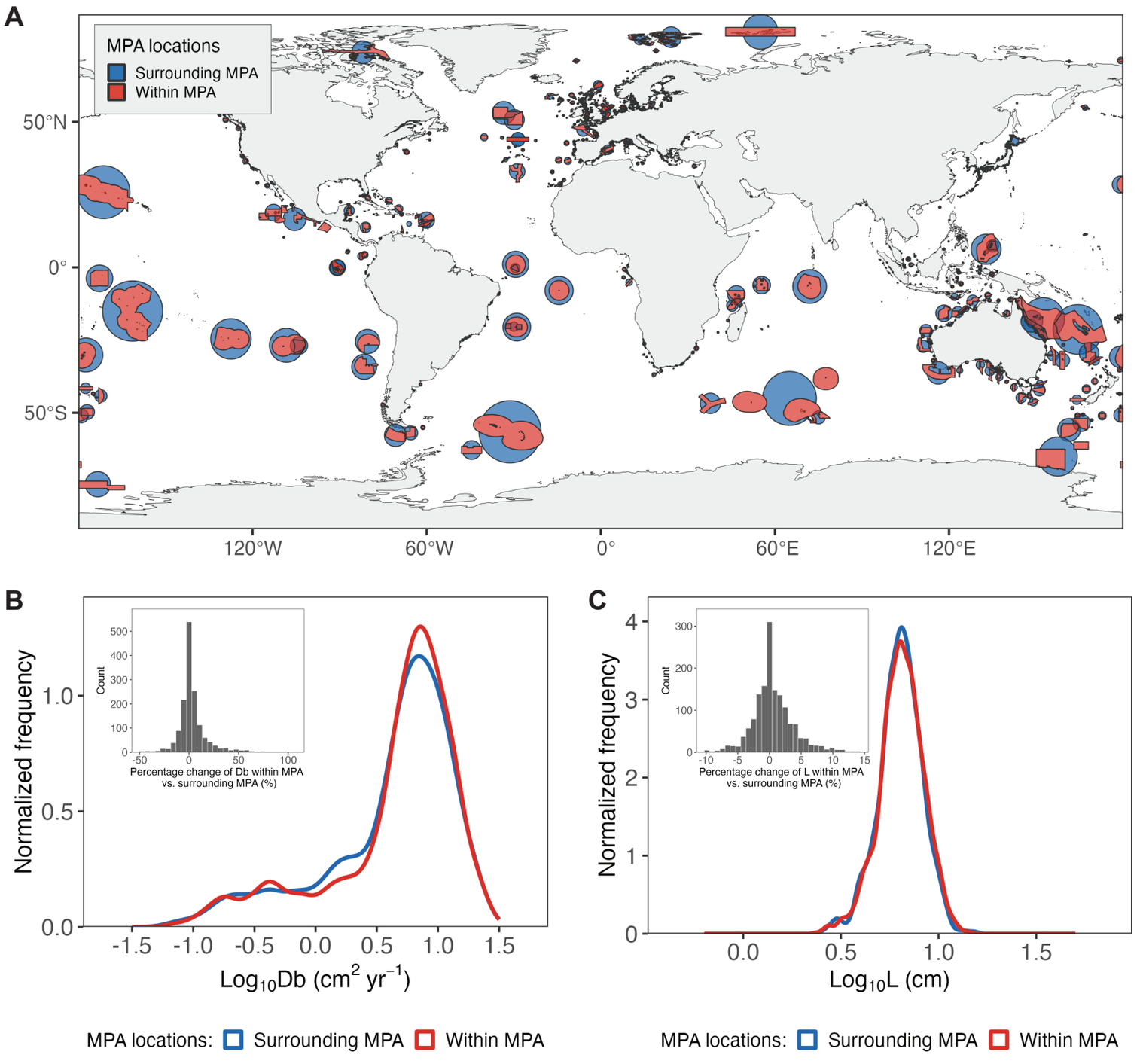
A
MPA locations
Surrounding MPA
Within MPA
50°N
0°
50°S
120°W
60°W
0°
60°E
120°E
B
Normalized frequency
Count
Percentage change of Db within MPA vs. surrounding MPA (%)
Log10Db (cm2 yr−1)
MPA locations: Surrounding MPA Within MPA
C
Normalized frequency
Count
Percentage change of L within MPA vs. surrounding MPA (%)
Log10L (cm)
MPA locations: Surrounding MPA Within MPA

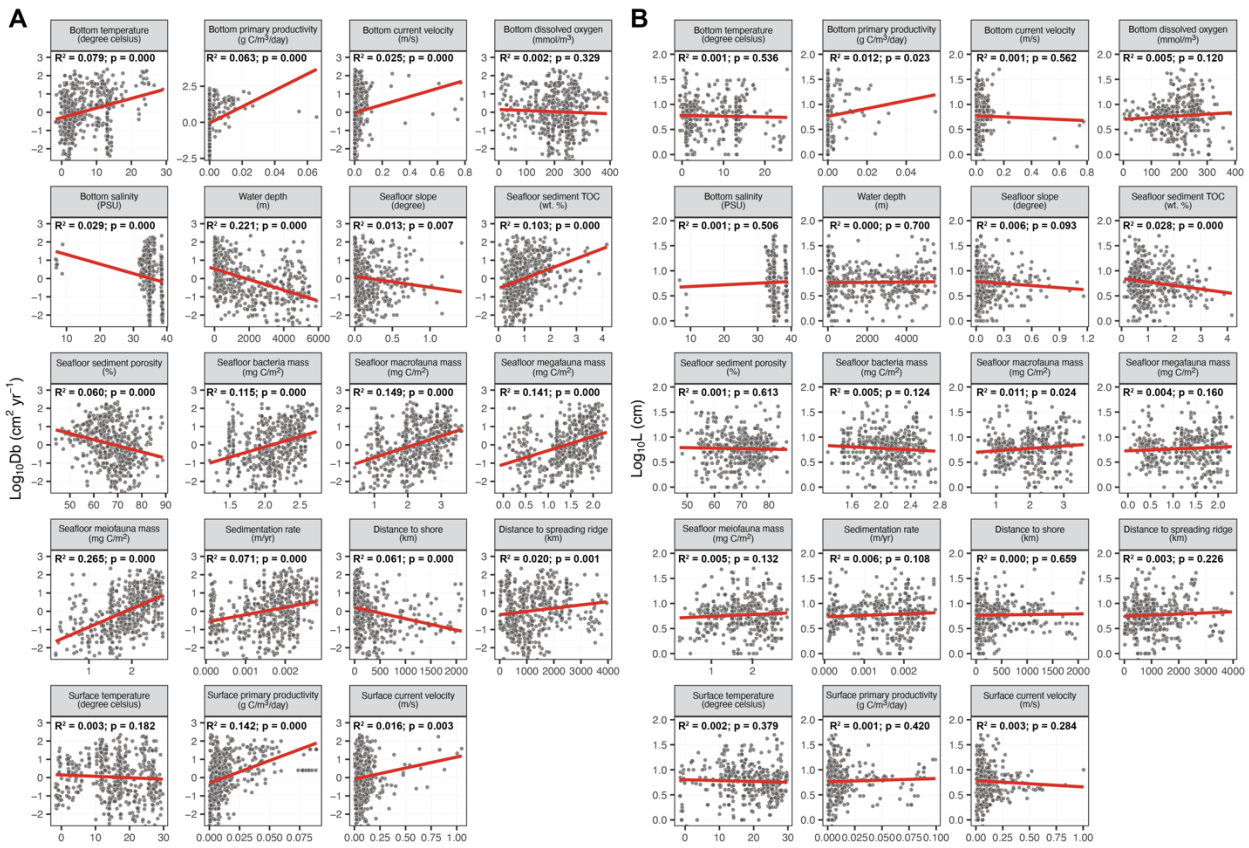

Figure S1. The relationship between bioturbation and spatially correlative environmental and ecological parameters. Related to Table S1 and Figure 2. (A) Bioturbation intensity (Db) (B) Mixed layer depth (L). In each panel, the red lines represent the linear regression between Db and the environmental and ecological parameters (shown solely for purposes of visualizing data trends). The associated R^2 value and p-value for each linear regression are noted in each panel. The source of each parameter is listed in Table S1.

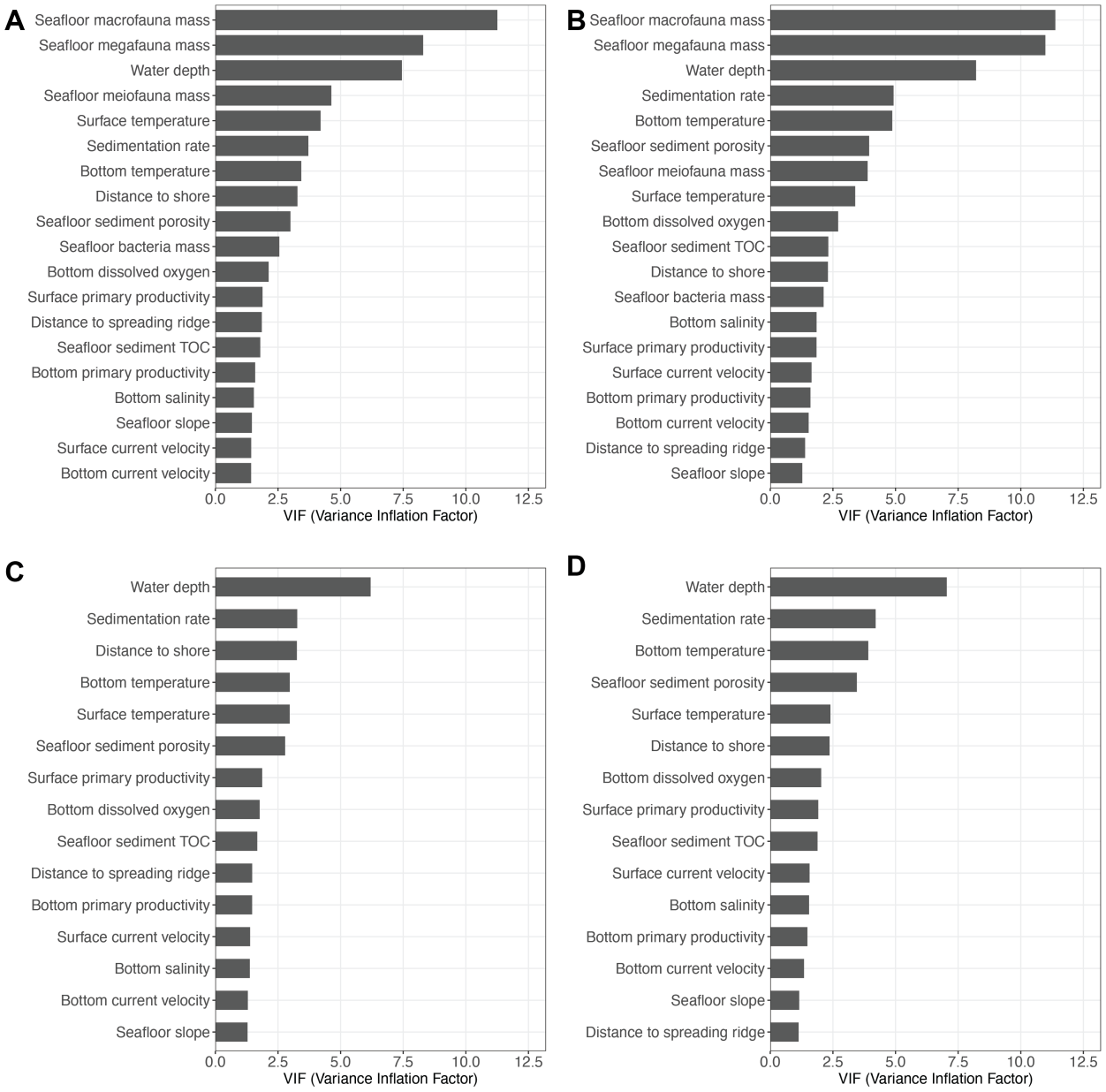

Figure S2. The Variance Inflation Factor (VIF) for predictor variables in the (A, C) Db and (B, D) L datasets. Related to Figure 2. The predictor variables include seafloor biomass parameters in (A) and (B) but exclude those parameters in (C) and (D).

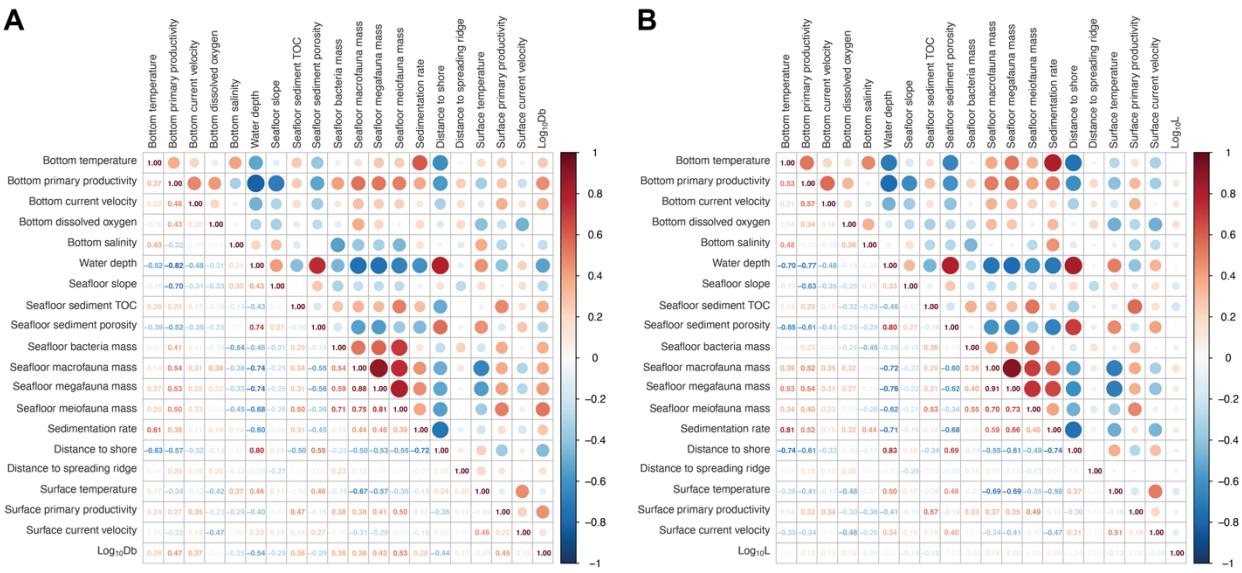

Figure S3. Pairwise spearman's rank correlation matrix of all spatially correlative environmental and ecological parameters and bioturbation. Related to Figure 2. We present the correlation matrix for (A) bioturbation intensity (Db) and (B) sediment mixed layer depth (L). Positive correlations are displayed in red and negative correlations in blue. Color intensity and circle diameter are proportional to the size of the correlation coefficients.

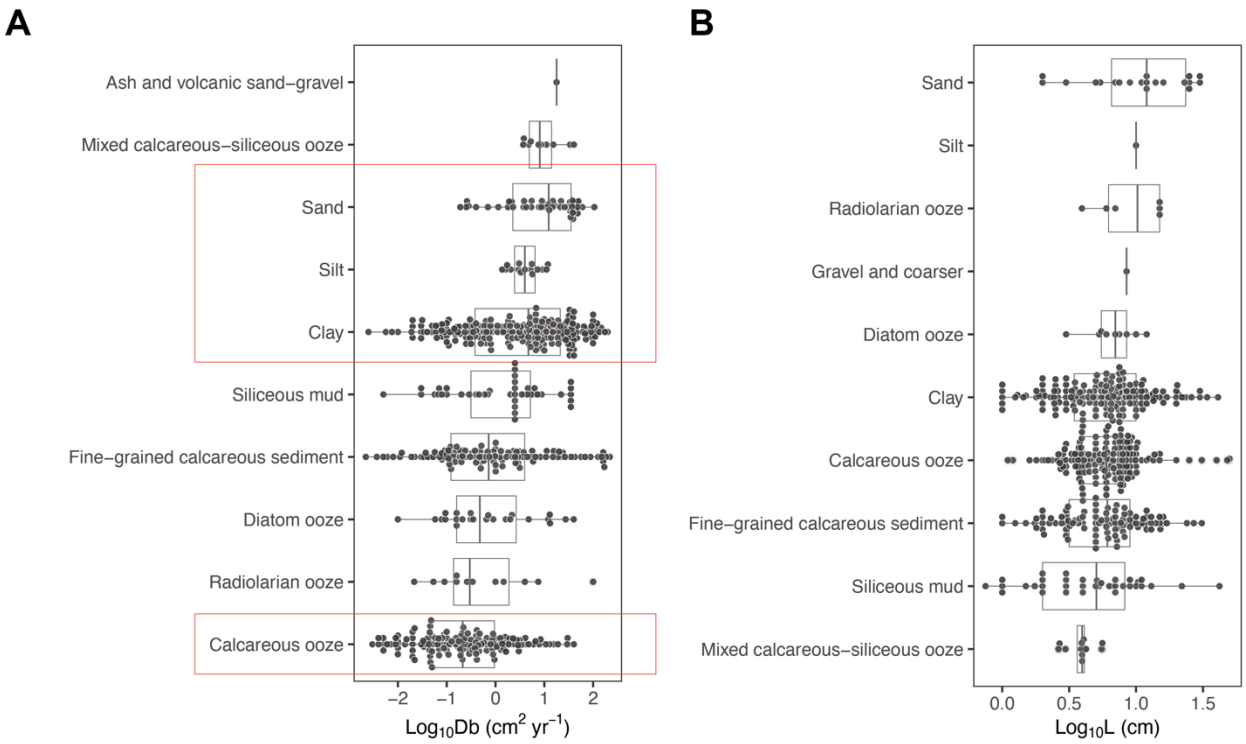

Figure S4. The relationship between seafloor sediment type and bioturbation (Db and L). Related to Figure 3. In each case, the median is indicated at the midpoint, the upper and lower quartiles are indicated by the box margins, horizontal lines represent the spread of the data outside the quartiles, and closed circles indicate individual observations. In panel (A), the upper red rectangle highlights siliciclastic sands, silts, and clays, which are associated with higher bioturbation intensities. Conversely, the lower red rectangle highlights biogenic calcareous ooze, associated with the lowest bioturbation intensities. In panel (B), no rectangles are displayed as no discernible relationship could be identified between sediment mixed layer depth and sediment type.

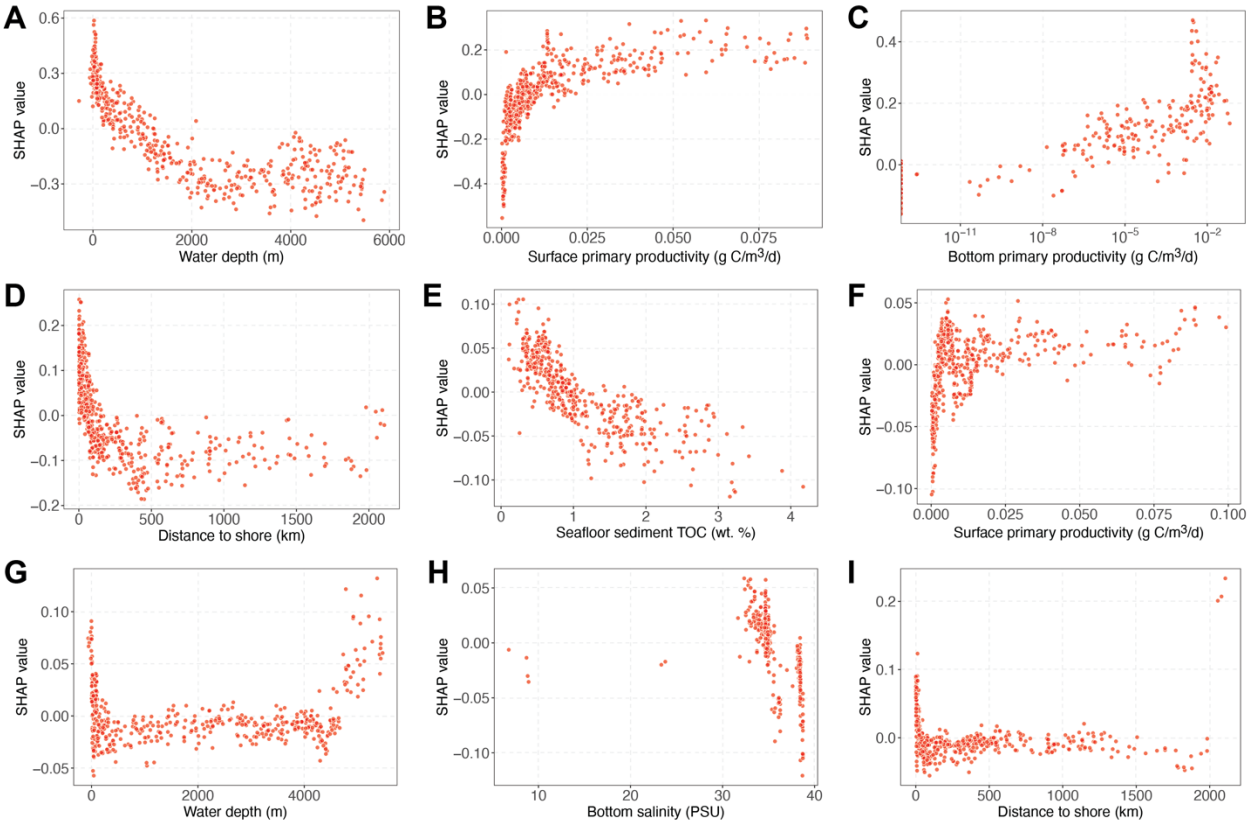

Figure S5. Relationship between SHAP values and the most important non-categorical predictor variables identified by machine learning. Related to Figure 4. (A–D) Relationship for Db. (E–I) Relationship for L. Features with positive SHAP values positively impact the prediction, while those with negative values have a negative impact. A positive correlation between a feature's values and its SHAP values can result in an increase in the prediction outcome as the feature value increases, while a negative correlation between a feature's values and its SHAP values can result in a decrease in the prediction outcome as the feature value increases.

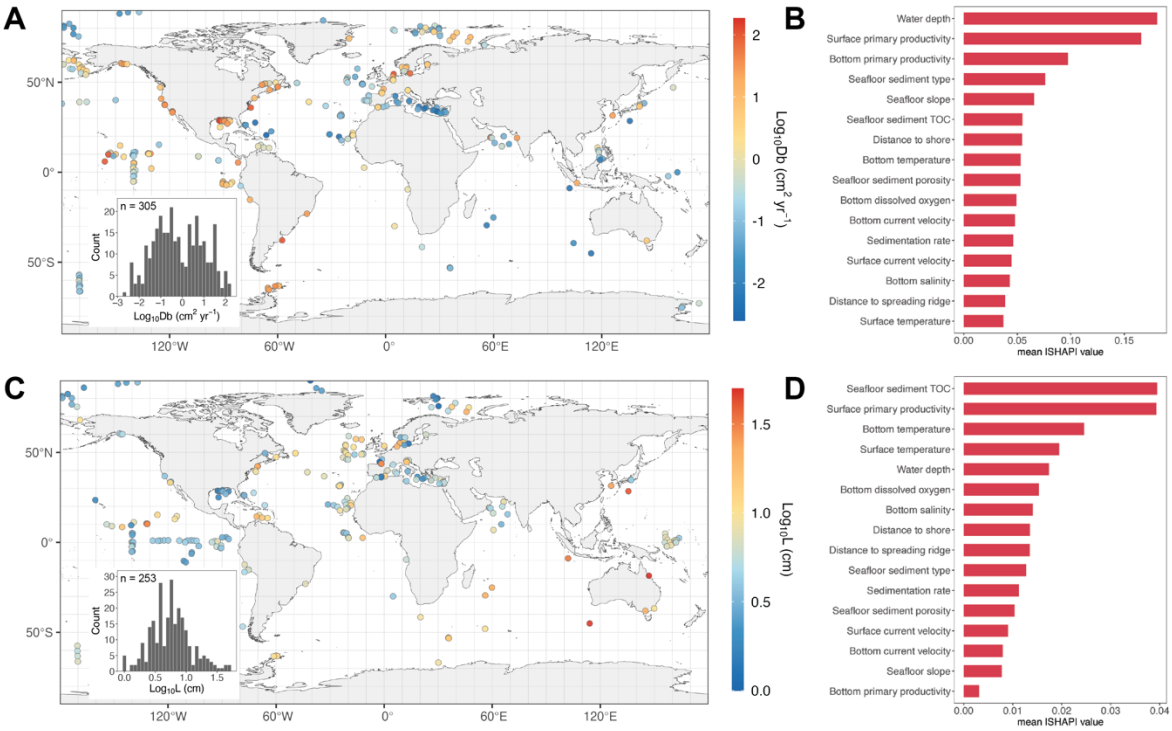

Figure S6. Distribution and machine-learning results for spatially weighted random sub-sampling of the full bioturbation dataset. Related to Figure 4. Site locations are shown for Db (A) and L (C). The mean absolute SHAP values (displayed in decreasing order, from top to bottom) associated with calculation of target variables Db (B) and L (D) from predictor variables are presented. We randomly sampled 50% of the entire Db or L dataset, with the selection probability scaled by the inverse density of samples within each 10×10˚ grid, across the entire global seafloor. The insets in (A) and (B) represent the histogram distributions of Db and L, with data split into 30 equal bins and the total number of observations indicated in the upper left portion of each inset.

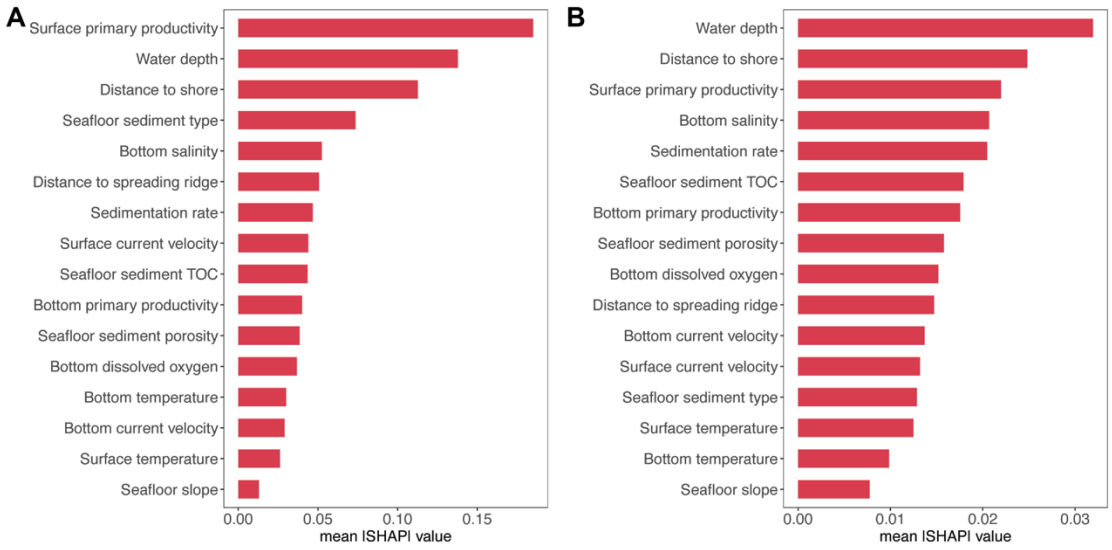

Figure S7. Machine-learning outcomes for Db and L for the screened ^{210}Pb data. Related to Figure 4. Mean absolute SHAP values (displayed in decreasing order, from top to bottom) associated with calculation of target variables Db (A) and L (B) from predictor variables are shown.

Variable Type	Database Name	Units	RMSE	R^2	Spatial Resolution	Time Span	Methods	Source
Environmental	Mean surface-water temperature	degree celsius	0.75	0.98	5 minutes	2000-2014	data re-analysis	S1
	Mean surface current velocity	m/s	-	-	5 minutes	2000-2014	data re-analysis	S1
	Mean bottom-water temperature	degree celsius	0.75	0.98	5 minutes	2000-2014	data re-analysis	S1
	Mean bottom current velocity	m/s	-	-	5 minutes	2000-2014	data re-analysis	S1
	Mean bottom-water salinity	practical salinity unit (PSU)	0.52	0.86	5 minutes	2000-2014	data re-analysis	S1
	Mean bottom-water dissolved oxygen concentration	$mmol/m^3$	23.5	0.92	5 minutes	2000-2014	biogeochemical model	S1
	Water depth	m	-	-	5 minutes	constant	empirical estimate	S1
	Seafloor slope	degrees	-	-	5 minutes	constant	empirical estimate	S1
	Seafloor sediment porosity	%	8.8	-	5 minutes	constant	machine learning	S2
	Seafloor sediment type	categories	-	-	6 minutes	constant	machine learning	S3
	Sedimentation rate	m/yr	-	-	1 degree	constant	empirical estimate	S4
	Minimum distance to spreading ridge	km	-	-	5 minutes	constant	empirical estimate	S2
	Minimum distance to shoreline	km	-	-	5 minutes	constant	empirical estimate	S1
Environmental/ Ecological	Mean surface-water primary productivity	$g\ C/m^3/day$	-	-	5 minutes	2000-2014	biogeochemical model	S1
	Mean bottom-water primary productivity	$g\ C/m^3/day$	-	-	5 minutes	2000-2014	biogeochemical model	S1
	Seafloor sediment TOC content	wt. %	-	0.61	5 minutes	constant	machine learning	S5
Ecological	Ocean ecoregion	categories	-	-	Shapefile	constant	empirical estimate	S6
	Ocean benthic biomass	$mg\ C/m^2$	-	0.8	1 degree	constant	machine learning	S7

Table S1 Summary of the source and spatial and temporal resolution of the environmental and ecological predictor variables used in data exploration and machine learning. "RMSE" represents Root Mean Squared Error. "R^2" represents the coefficient of determination. "Methods" denotes how these parameters were generated. Data either span specific periods of time (listed in the "Time Span" column) or record a static ("constant") snapshot. Cited references ("Source") listed at the end of this document as well as in the main text.

Algorithms	Hyperparameters	Ranges	R^2 for Db	R^2 for L
Random Forest	number of trees	500-1500	0.54	0.29
	minimal node size	1-10		
Support Vector Machine	kernel	linear, polynomial, radial, sigmoid	0.53	0.24
	epsilon	0.1-0.5		
	gamma	0.1-1		
ElasticNet Regression	s	0-15	0.46	0.09
	alpha	0-1		
K-Nearest Neighbors (KNN)	number of neighbors	1-20	0.52	0.21
Gradient Boosting	number of trees	500-1500	0.47	0.14
	maximum tree depth	1-10		

Table S2 Summary of the model performance of five machine-learning algorithms for the test data using R^2 value as a metric of relative performance. Note: For Random Forest, the "number of trees" parameter specifies the number of trees to be 'grown' in the model. The "minimal node size" parameter specifies the minimum number of observations that must exist in a node for it to be split further. For Support Vector Machine, the "kernel" parameter allows specification of which kernel function to use for the regression task. The "epsilon" parameter defines the width of the ε-insensitive loss function used in the regression. The "gamma" parameter is the kernel coefficient for the Radial Basis Function (RBF) kernel. For ElasticNet regression, the "s" parameter represents the regularization term λ in the elastic net penalty. It controls the amount of shrinkage applied to the coefficients, with higher values resulting in more regularization. The "alpha" parameter controls the mixing between L1 and L2 regularization. An alpha of 1 corresponds to Lasso regression (L1 regularization), and an alpha of 0 corresponds to Ridge regression (L2 regularization). Values between 0 and 1 are associated with a mixture of each. For K-Nearest Neighbors (KNN), the "k" parameter specifies the number of nearest neighbors to consider when making a prediction. For Gradient Boosting, the "number of trees" parameter specifies the total number of boosting iterations to be carried out or, equivalently, the total number of trees to fit. The "maximum tree depth" parameter specifies the maximum depth

of each individual regression estimation tree. For each algorithm, we iterated over a series of hyperparameter combinations within their ranges to find the optimal set. We then used the optimal set of hyperparameters to train each model and validate its performance (the R^2 value) using 10-fold cross validation.

Supplemental references

S1. Assis, J., Tyberghein, L., Bosch, S., Verbruggen, H., Serrão, E.A., and Clerck, O.D. (2018). Bio-ORACLE v2.0: Extending marine data layers for bioclimatic modelling. Glob. Ecol. Biogeogr. 27, 277–284. 10.1111/geb.12693.

S2. Martin, K.M., Wood, W.T., and Becker, J.J. (2015). A global prediction of seafloor sediment porosity using machine learning. Geophys. Res. Lett. 42, 10640–10646. 10.1002/2015GL065279.

S3. Dutkiewicz, A., Müller, R.D., O'Callaghan, S., and Jónasson, H. (2015). Census of seafloor sediments in the world's ocean. Geology 43, 795–798. 10.1130/G36883.1.

S4. Halevy, I., Fike, D.A., Pasquier, V., Bryant, R.N., Wenk, C.B., Turchyn, A.V., Johnston, D.T., and Claypool, G.E. (2023). Sedimentary parameters control the sulfur isotope composition of marine pyrite. Science 382, 946–951. 10.1126/science.adh1215.

S5. Lee, T.R., Wood, W.T., and Phrampus, B.J. (2019). A machine learning (KNN) approach to predicting global seafloor total organic carbon. Glob. Biogeochem. Cycles 33, 37–46. 10.1029/2018GB005992.

S6. Bailey, R.G. (2014). Ecoregions: The ecosystem geography of the oceans and continents 2nd ed. 2014 edition. (Springer).

S7. Wei, C.-L., Rowe, G.T., Escobar-Briones, E., Boetius, A., Soltwedel, T., Caley, M.J., Soliman, Y., Huettmann, F., Qu, F., Yu, Z., et al. (2010). Global patterns and predictions of seafloor biomass using Random Forests. PLOS ONE 5, e15323. 10.1371/journal.pone.0015323.